REPORT DOCUMENTATION PAGE	1 Form Approved OMB NO. 0704-0188

1. REPORT DATE (DD-MM-YYYY) 29-08-2014	2. REPORT TYPE Book Chapter	3. DATES COVERED (From - To) -

4. TITLE AND SUBTITLE Design and Applications of Nanomaterial-Based and Biomolecule-Based Nanodevices and Nanosensors	5a. CONTRACT NUMBER W911NF-11-1-0024
	5b. GRANT NUMBER
	5c. PROGRAM ELEMENT NUMBER 611103
6. AUTHORS Preeti Pratap, Justin Abell, Yiping Zhao, Barbara Nichols, Eugene Zakar, Michael Stroscio, Mitra Dutta, Ke Xu, Mohsen Purahmad, Kimber Brenneman, Xenia Meshik, Sidra Farid, Shripriya Poduri	5d. PROJECT NUMBER
	5e. TASK NUMBER
	5f. WORK UNIT NUMBER

7. PERFORMING ORGANIZATION NAMES AND ADDRESSES University of California - Irvine 5171 California Ave., Suite 150 Irvine, CA 92697 -7600	8. PERFORMING ORGANIZATION REPORT NUMBER
9. SPONSORING/MONITORING AGENCY NAME(S) AND ADDRESS (ES) U.S. Army Research Office P.O. Box 12211 Research Triangle Park, NC 27709-2211	10. SPONSOR/MONITOR'S ACRONYM(S) ARO
	11. SPONSOR/MONITOR'S REPORT NUMBER(S) 58162-EL-MUR.77

12. DISTRIBUTION AVAILABILITY STATEMENT

Approved for public release; distribution is unlimited.

13. SUPPLEMENTARY NOTES

The views, opinions and/or findings contained in this report are those of the author(s) and should not contrued as an official Department of the Army position, policy or decision, unless so designated by other documentation.

14. ABSTRACT

see attached

15. SUBJECT TERMS

DNA, Nanotechnology

16. SECURITY CLASSIFICATION OF:			17. LIMITATION OF ABSTRACT	15. NUMBER OF PAGES	19a. NAME OF RESPONSIBLE PERSON
a. REPORT	b. ABSTRACT	c. THIS PAGE			Peter Burke
UU	UU	UU	UU		19b. TELEPHONE NUMBER 949-824-9326

Report Title

Design and Applications of Nanomaterial-Based and Biomolecule-Based Nanodevices and Nanosensors

ABSTRACT

see attached

Chapter 3
Design and Applications of Nanomaterial-Based and Biomolecule-Based Nanodevices and Nanosensors

Ke Xu, Mohsen Purahmad, Kimber Brenneman, Xenia Meshik, Sidra Farid, Shripriya Poduri, Preeti Pratap, Justin Abell, Yiping Zhao, Barbara Nichols, Eugene Zakar, Michael Stroscio and Mitra Dutta

Abstract This review will highlight recent research underlying the design of novel nanodevices and nanosensors that incorporate graphene, nanodots, nanowires, and biomolecules including DNA aptamers and peptides. The emphasis is on models and theory that guide the design of these nanodevices and nanosensors. In selected cases, research designed to test the usefulness of these designs is highlighted in this chapter.

3.1 Introduction

The design considerations and applications of nanomaterial-based and biomolecule-based nanodevices and nanosensors vary greatly from one specific nanosystem to another. Herein, a selection of such nanodevices and nanosensors are highlighted

---

M. Stroscio (✉) · K. Xu · M. Purahmad · S. Farid · S. Poduri · M. Dutta
Electrical and Computer Engineering Department, University of Illinois at Chicago (UIC), 851 S. Morgan Street, Chicago IL 60607, USA
e-mail: stroscio@uic.edu; m.stroscio@frontier.com

K. Brenneman · X. Meshik · P. Pratap · M. Stroscio
Bioengineering Department, University of Illinois at Chicago,
851 S. Morgan St., Chicago IL, USA

J. Abell
Nanoscale Science and Engineering Center, Department of Biological and Agricultural Engineering, The University of Georgia, Athens GA, USA

Y. Zhao
Nanoscale Science and Engineering Center, Department of Physics and Astronomy,
The University of Georgia, Athens, GA, USA

B. Nichols · E. Zakar
SEDD Directorate, US Army Research Laboratory, Adelphi, MD, USA

M. Stroscio · M. Dutta
Physics Department, University of Illinois at Chicago,
851 S. Morgan Street, Chicago, IL, USA

J. M. Seminario (ed.), *Design and Applications of Nanomaterials for Sensors,*
Challenges and Advances in Computational Chemistry and Physics 16,
DOI 10.1007/978-94-017-8848-9_3,

and a combination of theoretical considerations and empirical observations are invoked to guide the design on a case-by-case basis. Among the nanosystems considered are: biomolecule-based sensors with active biomolecule elements anchored on graphene-like surfaces; nanowires with strong piezoelectric interactions in the presence of depletion regions; systems with quantum-dots in contact with semiconductor substrates; nanowire polarizers; indirect bandgap semiconductors bound to DNA as a means of realizing light-induced cleaving of DNA; and nanosencors incorporating surface-enhanced Raman scattering. In each case specific design considerations and background materials are discussed.

3.2 Design of Aptamer-Based Sensors with Graphene and Carbon Nanotube Substrates

Herein, the design of aptamer-based sensors with graphene and carbon nanotube substrates is surveyed. In order to design such devices, it is necessary to consider the underlying mechanisms and principles by which these aptamer-based sensors function. Aptamers are short strands of specific oligonucleic acid sequences containing about 30–80 oligonucleotides. Aptamers can recognize specific ligands or analytes and bind to various target molecules ranging from small ions to large proteins with high selectivity and affinity. In 1990 within a short period of time, three groups independently developed in vitro selection and amplification technique for the isolation of specific nucleic acid sequences able to bind to target molecules with high affinity and specificity [1–3]. Both RNA and DNA aptamers are found and selected by a process called SELEX (Selection Evolution of Ligands by Exponential Enrichment) from vast populations of random sequences. Aptamers are sometimes called synthetic antibodies because they have similar properties in a number of applications.

Biosensors are integrated devices capable of detecting the presence of a target by using a particular recognition element and then providing quantitative or semi-quantitative analytical information. Biosensors detect the target analyte by monitoring the mass, optical or electronic signal changes induced by the interaction between the recognition element and the target analyte. When the recognition component of the biosensor is an aptamer it is also called an aptasensor [4]. Aptamer-based biosensors can takes advantage of the high affinity and tunable properties of aptamers. Comparing with antibodies, aptamers have a wide range of advantages such as smaller size, ability to be labeled without affecting affinity, ability to bind with drugs and toxic substance, etc.

3.2.1 Considerations Underlying the Design of Optical Aptamer-Based Biosensor

Fluorescent detection is the most used technique in aptamer-based bio-recognition of optical bioassays. Aptamers can be easily labeled with fluorescent dyes and functionalized with different fluorophores as well as quenchers. Fluorescent detection also has the advantage of inherent capability for real-time detection.

One of the first examples of an optical aptamer-based sensor was discovered by Kleinjung et al. [5] for the detection of L-adenosine. They immobilized a biotinylated RNA aptamer on streptavidin-derivatized optical fibers. The approach made evaluation of the association and dissociation kinetic possible and showed the capability of aptamers for the sub-micron detection of specific analytes. Several other approaches have been developed for converting aptamers into fluorescent signaling probes. A frequently adopted method is aptamer-based molecular beacons. A molecular beacon is a nucleic acids probe that is able to undergo spontaneous conformational change when encountering their complementary nucleic acid targets and translate the conformational change into a change in fluorescent properties. An aptamer-based molecular beacon is a modified version of traditional molecular beacon and usually called aptabeacon [6]. It places an aptamer sequence in a molecular beacon-like hairpin structure, and terminated the ends with a fluorophore and a quencher, respectively. Theoretically, any known aptamer can be engineered into a molecular aptamer beacon by adding a small nucleotide sequence to its 5′-end as well as a small sequence added to its 3′-end [6]. A fluorophore can then be covalently added to the 5′-end, and a quencher can be attached to the 3′-end. In the absence of target ligand, the beacon will form into a stem structure, resulting in the fluorophore and quencher to be close to each other. This time there will be no fluorescence signal because the fluorophore is quenched by energy transfer to the quencher. When the ligand is present, the aptamer will bind to the target ligand and forming a probe. The binding of target is stronger and more stable than the stem and thus it can disrupt the stem, open the structure, separate quencher from the fluorophore and leading to fluorescence signals that is able to be measured quantitively or semi-quantitively [7].

3.2.2 Electrochemical Aptamer-Based Biosensor

Typical electrochemical aptamer-based biosensors operate by reacting the aptamer with an analyte of interest and producing an electrical signal proportional to the analyte concentration. The electrochemical aptamer-based biosensors can be divided into three major types based on the assay format and the method of detection. The first type is sandwich and competition-type assays, in which an electrode-bound aptamer is used to bring a complex composed of the target and some redox-active analytes to the electrode. The second type involves the use of electrochemical impedance spectroscopy to detect targets adsorbed onto an aptamer-terminated electrode surface. And the third type utilizes electrochemistry to monitor binding-related conformational changes in an electrode-bound aptamer.

In a typical beacon format, Xiao et al. [8] reported detection based on a 3-D conformational change with thrombin binding where the aptamer undergoes a structural rearrangement. The conformational change allows thrombin detection with a beacon that does not require a stem-loop. Thrombin is a proteolytic enzyme which facilitates blood clotting by converting fibrinogen into fibrin, which is also used as a tumor marker in the diagnosis of pulmonary metastasis. The aptamer molecular beacon was constructed [8] by attaching a methylene blue molecule to one end of the aptamer and a thiol group to the other end. The thiol group is used as a linker for its immobilization on a gold electrode surface. Before interaction with thrombin, the aptamer was elastically able to interact with the electrode surface and transferring electrons. However, after interaction occurred, a longer electron-tunneling distance was created, and thus decreasing the signal. A similar aptamer molecular beacon approach was used by the team for the electrochemical detection of platelet-derived growth factor in picomolar levels, and demonstrated this aptamer-based biosensor directly in blood serum [9].

A difficulty with sandwich assays was later removed by Radi et al. [10], who developed "signal-on" architecture rather than the "signal-off" architecture, in which the binding of the target analyte resulted in a decrease in the signal. In this case, the aptamer molecular beacon had a ferrocene label and a shorter spacer. Detection was carried out using cyclic voltammetry, DPV and impedance measurements. In the absence of thrombin the ferrocene label is far from the electrode surface and would not provide any electron transfer to the surface. When thrombin is present, G-quadruplex would form leading to the ferrocene label close enough to the electrode and allowing effective electron transfer as well as signal generation. With the use of DPV a detection limit of 0.5 nM was achieved with a linear range of 5–35 nM. Xiao et al. [11] made similar efforts to modify their previous structure and fabricate "signal-on" electrochemical aptamer sensor. They introduced double-stranded DNA consisted of a short DNA sequence tagged with methylene blue (MB) that can hybridize with an aptamer, and a sequence complementary to it which contained the anti-thrombin aptamer sequence. The duplex of DNA maintained the redox label at "standing" position with a distance from the electrode surface. When thrombin is introduced to the complex, the complementary sequence would displaced and the MB tagged single stranded DNA would approaches the electrode surface and producing electric current due to improvement of electron transfer.

3.2.3 Graphene and Graphene-Based FET Structure

Graphene is a two-dimensional network of single layer sp^2-bonded carbon atoms arranged on a honeycomb lattice. The name graphene is sometimes used to describe multiple layer graphite. Multilayer graphite can have up to ten layers and still be called graphene. It should be noted that the variation in properties of graphene is quite significant when going from one layer to several layers. Ten layers is the limit where graphene becomes graphite, which is stack of graphene sheets bounded by weak van der Waals forces.

The atomic structure of graphene gives rise to exceptional electrical, optical, mechanical and thermal properties [12]. The most interesting electrical properties of graphene are high electron mobility [13] and ballistic transport of charge carriers

[14]. The high mobility is caused primarily by the absence of backscattering due to the pseudo spin nature of the charge carriers in graphene similar to the case of the carbon nanotube (CNT) [15]. Weak electron-phonon coupling, high sound velocity, and the near defect-free lattice also contribute to the high mobility and high current density sustainability of graphene. Graphene can sustain high current density up to 5×10^8 A/cm^2, or about 1 uA per atomic row of carbon atoms [16]. Ballistic transport over sub-micron scales is usually associated with high mobility and the quantization of conductance in narrow channels [14]. Also, graphene technology can be easily integrated into the existing planar processing infrastructure, grown on numerous substrates such as silicon dioxide, and processed by conventional semiconductor methods. Due to graphene's unique electronic properties, ultrafast electronic devices with operating frequencies up to THz are expected.

These properties of graphene come from its special bank structure. Graphene is a zero-bandgap semiconductor. In other words, it's both a semiconductor and a semi-metal. Theoretically, Wallace [17] first studied the band structure of graphene and demonstrated its unusual semi-metallic behavior. The lack of a bandgap in intrinsic graphene is a major engineering issue. The zero-bandgap means that graphene is difficult to be switched off (from conductive state to non-conductive state). Graphene nanoribbons or bilayer graphene are good alternatives to circumvent this problem, both of them can have a band gap and being tuned to meet the requirements of a solid state switch. Nevertheless, the zero-bandgap of large area graphene is not an issue in radio frequency (RF) applications.

Applications of graphene include many fields such as graphene thin film electrodes, using graphene as sensing material, graphene-based nanocomposites and graphene-based field-effect transistor (GFET) [18, 19]. A field-effect transistor (FET) is an electronic device normally with three terminals. The conductivity between two of the terminals known as source and drain can be controlled by the electric field created by the third terminal known as gate. Gate voltage can be tuned to modulate the free carrier density in the channel between source and drain, leading to a current change in the channel controlled directly by gate voltage. This shift of current can be used as a switch which indicates an "On" state when the current is in high value and an "Off" state when very low current is in the channel. The semiconductor industry is considering GFET as a possible alternative to replace the silicon field-effect transistor [20]. Carbon nanotubes offer similar electronic properties as graphene and had been considered as a replacement for silicon for years. But the fact that graphene has planar geometry and thus can be processed with more conventional complementary metal oxide semiconductor (CMOS) technology gives it a significant advantage over CNTs. The structure of a GFET is identical to a silicon FET.

Figure 3.1 shows a typical current (I_{SD})/voltage (V_{SD}) characteristics of chemically converted graphene devices. Single layer and bilayer graphene were grown in collaboration with Army Research Laboratory using low pressure chemical vapor deposition (LPCVD) and transferred to Si/SiO$_2$ substrate. The thickness of graphene was later confirmed with Raman spectroscopy to be consisting of 94 % bilayer and 6 % single layer graphene. The FET structure is fabricated with chromium

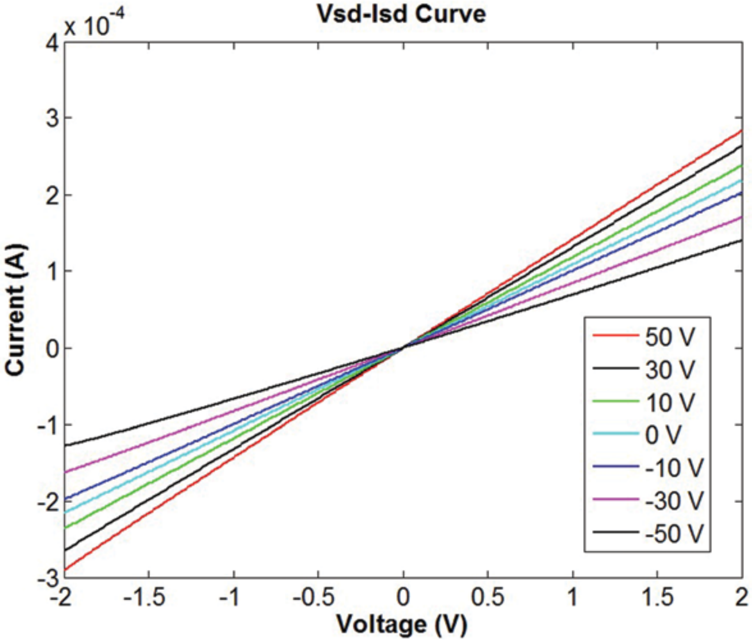

Fig. 3.1 Current voltage characteristic of a graphene-based FET structure

and gold as source and drain electrodes. Current between source and drain can be effectively modulated by gate voltage. When the gate voltage varied from 50 to −50 V, the conductance of the device increased, indicating a p-type semiconductor under ambient conditions.

3.2.4 Aptamer-Based Sensors with Graphene and CNT Substrates

Since the first biosensor with Si nanowire was reported in 2001 [21] and the development of the chemical sensor using carbon nanotubes in 2000 [22], massive research efforts have been initiated in developing nanowire-based or nanotube-based sensors. In the case of carbon nanotubes, all constituent atoms are at the surface and any small change on the surface can lead to a large change in electrical current, which made possible of developing sensors with exceptional sensitivity.

So et al. fabricated a single-walled carbon nanotube (SWNT) field-effect transistor to monitor the binding processes between aptamer and protein [23]. SWNTs behave as p-type semiconductors in ambient atmosphere. The merit of using aptamers in FET-based sensor lies in their small size. Debye length is defined as the typical distance required for screening the surplus charge by the mobile electric

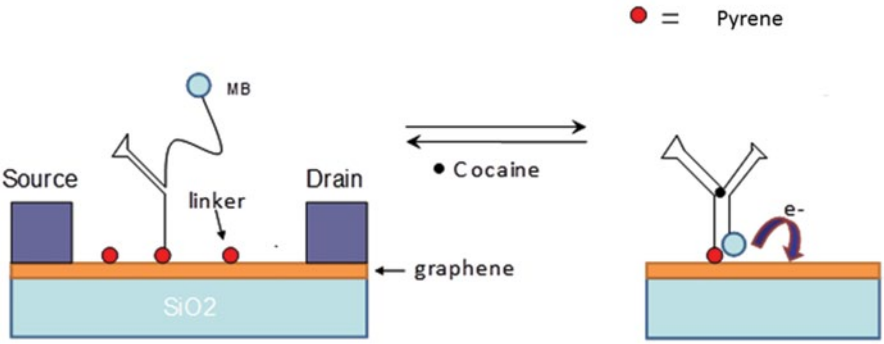

Fig. 3.2 Device schematic of a aptamer-based biosensor with graphene-based FET structure

carrier present in a nanostructure. The size of antibodies is about 10 nm, which is much larger than the Debye length or electrical double layer that is about 3 nm in 10 mM ionic concentration. As a result, the recognition of protein-protein binding process might occur outside the electrical Debye length and left very weak potential changes to be observed on the gate. Aptamers, on the other hand, have an average of 2 nm for 30 bases, which is within the Debye length and can enable the perturbation of gate potential by proteins that link to aptamers. SWNTs were deposited between source and drain electrodes, and anti-thrombin aptamers were attached on the CNTs. The binding of thrombin to the aptamer altered conductance between source and drain, thus enabling detection of the protein.

The applications of SWNTs, however, are often plagued with several problems. For example, it is difficult to separate metallic nanotubes from semiconducting nanotubes. Also, when only a few SWNTs are used, it is challenging to manipulate them for device fabrication because they are too small to interface with large-sized biomolecules. Graphene, with similar properties as SWNT but comes in a flat structure, has many advantage in fabricating sensors.

Figure 3.2 is an example of aptamer-based sensor with graphene FET structure using cocaine as a target. The aptamer is terminated with methylene-blue (MB) which functions as an electron donor. 1-pyrenebutanoic acid, succinimidyl ester (merchandise name: P130) as the red dot in the figure is used as linker molecule to noncovalently bind the aptamer to the graphene surface by the pyrene group in the linker. Due to the overlapping of π-bonds between aromatic side chains, the pyrene group which is highly aromatic in nature could interact strongly with the basal plane of graphite via π-stacking. The cocaine aptamer is about 2-nm in length with 30 bases, which is less than the Debye length. When the target molecule is present, the aptamer will undergo a conformation change and lead to a closer distance between the MB and the graphene surface. When the MB approaches the surface, it can provide excess electrons and cause a shift in the I-V characteristics of the graphene-FET. It is known that electrical contacts to a graphene surface typically exhibit high resistance. This is possibly due to the weak electron conduction on the interface. The electronic structure and the weak van der Waals binding can cause relatively small matrix elements for electrons to cross the interface. When conduct the device characteristic calculations using a p-type MOSFET model, after the formation of inversion layer the net charge carrier density will reduce due to the external excess charge. We can assume,

$$Q(Net) = Q_p - Q_{ext}, \tag{3.1}$$

where Q_p is the inversion charge and Q_{ext} is the extra electron charge provided by methylene blue. At equilibrium, the inversion layer charge in MOS-C will balances the charge added to the gate when V_G exceeds V_T. Therefore,

$$Q_p = -Q_{gate} \cong -C_o \Delta V_G = -C_o (V_G - V_T). \tag{3.2}$$

The external charge Q_{ext} depends on the concentration of cocaine. More cocaine molecules near the structure will cause more aptamers to make the conformational change, leading to additional electron charge at the surface. Since the current flow in the conducting channel is almost exclusively in one direction (taken to be y direction), and since the diffusion current is usually negligible compared with more numerous carriers at a certain point, the equation can be simplified to

$$J_p = q\mu_p p\varepsilon = -q\mu_p p \frac{d\phi}{dy}. \tag{3.3}$$

where μ_p is the mobility of holes. The effective mobility may be defined as

$$\overline{\mu_p} = -\frac{q}{Q_{N(y)}} \int_0^{x_c(y)} \mu_p(x,y) p(x,y)\, dx. \tag{3.4}$$

Integrating I_D over the length of channel gives

$$\int_0^L I_D\, dy = I_D L = -Z \int_0^{-V_D} \overline{\mu_p} Q_p\, d\phi \tag{3.5}$$

$$I_D = -\frac{Z\overline{\mu_p}}{L} \int_0^{-V_D} Q_p\, d\phi. \tag{3.6}$$

where Q_p is the positive charge/cm^2 in the channel. In this model, due to the existence of excess electron charges provided by methylene blue,

$$Q_p(Net) = -C_0 (V_G - V_T - \phi) - Q_{ext}, \tag{3.7}$$

where Q_{ext} is the trapped external charge from MB. From the two equations above, we obtain the $I_D - V_D$ relation as

$$I_D = \frac{Z\overline{\mu_p}C_0}{L}\left[(V_G - V_T)V_D - \frac{V_{D^2}}{2}\right] - \frac{Z\overline{\mu_p}V_D}{L}Q_{ext}. \tag{3.8}$$

Similar structure had also demonstrated by Huang et al. [24] who used large-sized CVD grown graphene films to configure field-effect transistors for real-time biomolecular sensing. Glucose or glutamate molecules were detected by the conductance change of the graphene transistor as the molecules are oxidized by the specific redox enzyme (glucose oxidase or glutamic dehydrogenase) which functions as mediator to attach to the graphene surface. These results from current aptamer-based biosensors with graphene-based structure show exceptional electronic response and the ability to support cell adhesion and growth, which postulates the promising potentials of graphene in nanoelectronic biosensing as well as applications in interfacing with living cells and detecting dynamic bimolecular analytes.

3.3 Design Concepts of Nanoscale Piezoelectric Structures

Recent advancements in portable and lightweight mobile devices, has led to needing alternate power sources instead of conventional batteries. Batteries are not feasible in many applications because of their lifetime, weight, size, safety and for use in remote locations. There are emerging applications such as biomedical drug-delivery implants, implantable medical electronic devices and wireless micro-sensor networks, where conventional batteries are impractical because of the difficulty in replacing the batteries [25–28]. Several energy sources such as solar, thermal and mechanical energy can be used as sources of energy in self-powered devices. However, using the mechanical energy has garnered significant attention in self-powered devices, as such a source is commonly available in small-scale systems. Taking the forms of irregular air flow/vibration, ultrasonic waves, body movement, and hydraulic pressure, mechanical energy is pervasive and accessible from the surrounding environment. From this point of view piezoelectric elements are among the best candidates due to their unique properties such high energy densities and integration potential which make them promising for the design of self-powered small-scale devices [28, 29]. The schematic diagram of a vibration energy harvesting system is shown in Fig. 3.3. The conversion of mechanical energy to electrical energy has been well demonstrated using piezoelectric cantilever-based microelectromechanical (MEMS) devices working at their resonating mode [30]. However, the large unit size, large triggering force and specific high resonance frequency of the traditional cantilever-based energy harvester limit their applicability and adaptability in nanoscale devices and systems. In this domain, one dimensional (1D) nanostructures

Fig. 3.3 Schematic diagram of a vibration energy harvesting system

have attracted much attention in the fabrication of nanogenerators. Recently, it has been demonstrated that nanogenerators (NGs) based on piezoelectric nanowires (NWs) have the potential to harvest mechanical energy [29]. The first nanoscale energy harvester based on ZnO NWs was introduced by Wang et al. [31]. Among the piezoelectric nanostructures such as lead zirconate titanate (PZT) NWs and Polyvinylidene fluoride (PVDF) nanofibers, the piezoelectric semiconductor nanowires such as ZnO NWs and GaN NWs have been the focus of considerable research.

Because piezoelectric semiconductors can be used to convert mechanical energy to electrical energy and also since they are semiconductors, they can be used as a junction device for performing diode and transistor-type functions. These properties make them strong candidates for use in electromechanically coupled sensors and transducers [31, 32]. However, due to the presence of free carriers in semiconductor piezoelectric materials the physics behind the semiconductor nanogenerators such as ZnO NWs is not well known [33]. Hence, the application of piezoelectric semiconductor nanowires (NWs) requires a good understanding of their electrical and piezoelectric properties. Herein, one of the main concepts for design of ZnO NWs-based nanogenerators (NGs) is addressed.

3.3.1 Fundamentals of Piezoelectricity

The origin of piezoelectricity effect is the displacements of ions in the crystal by an induced strain. This effect is seen for crystal structures with no center of symmetry. Since compound semiconductors such as ZnO usually belong to non-centrosymmetric crystal groups, they are piezoelectric materials. The crystal symmetry of ZnO is responsible for the different components of the internal polarization, spontaneous polarization and piezoelectric polarization. The charge produced by the piezoelectric effect is a bound charge (polarization or dielectric displacement) and the piezoelectric strain equations can be described as follows [33, 34].

$$\begin{aligned} T &= -e.E + c^{E} : S \\ D &= \varepsilon^{S}.E + e : S \end{aligned} \tag{3.9}$$

where T is the stress, c is the elastic stiffness constant, e is the polarization constant, E is the electric field, D is the electric displacement, S is the strain and, and ε is the electric permittivity. However, the above equations are valid in the case of an ideal insulator, in which the density of free carriers is zero or negligible. In this case, the generation of the piezoelectric charge might be considered equivalent to the generation of an electrical field or a potential. Therefore, in the case of a piezoelectric semiconductor, such as ZnO NWs, the piezoelectric constitutive equations cannot be applied directly due to the presence of free carriers [33]. In the non-depleted region of a piezoelectric semiconductor the free carries migrate to the region where piezoelectric polarization appears to maintain the quasi-neutrality. The migration time of free carries is on the order of the dielectric relaxation time. However, in the depletion region of a semiconductor, where the density of free carriers is negligible, the piezoelectric charges may be added to the ionized impurities (donors or acceptors) [35].

3.3.2 Piezoelectricity Effect in 1D Piezoelectric Semiconductor Nanostructures

In case of 1D nanostructures such as ZnO NWs where the ratio of surface to volume is high, the surface the adsorbed species such as O_2 molecules undergo chemisorption on the surface of the NW by capturing a free electron from the n-type ZnO result in a surface depletion region [36]. In Fig. 3.4, the schematic representation of a single nanowire and its band bending is depicted, the radius of non-depleted region is r_{elec} and the depletion region width is d. As discussed above, in the depleted region of a piezoelectric semiconductor, the generation of the piezoelectric charge might be considered equivalent to the generation of an electrical field or a potential. Hence, in the surface depletion region of a ZnO NW where the density of free carriers is negligible, the piezoelectric strain equations can be applied. In a detailed study [37], by considering a non-depleted region and a surface depleted region in a ZnO NWs and solving the Poisson equation in radial coordinate system, the effect of induced piezoelectric charges on the surface potential of ZnO NWs have been investigated. The surface depletion width (d) in 1D structure shown in Fig. 3.2 can be described as given [37]:

$$d = r_{phys} - \sqrt{r^2{}_{phys} - \frac{2r_{phys}q^2 D_{it}\psi_0}{\rho\left(1 + \frac{r_{phys}q^2 D_{it}}{2\varepsilon_s}\right)}} \tag{3.10}$$

where D_{it} is the interface state density and

$$\rho(r) = q\left[N_v \exp\left(\frac{-E_g}{2KT}\right)\exp\left(\frac{-q}{KT}\psi_r\right)\right.$$
$$\left. - N_c \exp\left(\frac{-E_g}{2KT}\right)\exp\left(\frac{q}{KT}\psi_r\right) + N_D - N_A\right]$$

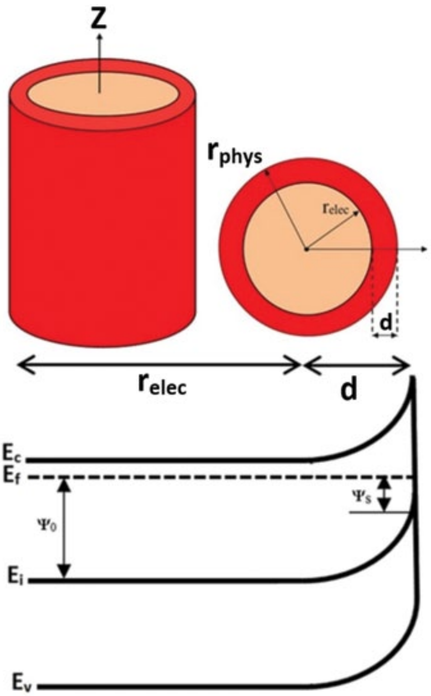

Fig. 3.4 Schematic representation of the nanowire and its band bending

By solving the Poisson equation in a radial coordinate system, the electrostatic potential in surface depleted region can be expressed as shown below [37]:

$$
\begin{aligned}
&\psi(r) = \psi_o && 0 \le r \le r_{relec} \\
&\psi(r) = \psi_o - \frac{eN_D}{4\varepsilon}\left(r^2 - (r_{Phys} - d)^2\right) && \\
&\qquad + \frac{eN_D}{2\varepsilon}(r_{Phys} - d)^2 \left(Ln\left(\frac{r}{r_{Phys} - d} \right) \right) && r_{elec} \le r \le r_{phys}
\end{aligned}
\tag{3.11}
$$

Considering a uniform plane wave propagating with an arbitrary angle in the XZ plane of a wurtzite crystal the radial piezoelectrically induced polarization component can be expressed as follows [38]:

$$
\begin{aligned}
p_r = {} & (e'_{x1}\cos^3\Phi + e'_{x2}\cos\Phi\sin^2\Phi + e'_{y6}\sin\Phi\sin 2\Phi)\frac{\partial u_r}{\partial r} \\
& + (e'_{x1}\cos\Phi\sin^2\Phi + e'_{x2}\cos^3\Phi - e'_{y6}\sin\Phi\sin 2\Phi)
\end{aligned}
\tag{3.12}
$$

$$
\begin{aligned}
&\times\left(\frac{u_r}{r}+\frac{1}{r}\frac{\partial u_r}{\partial \Phi}\right)+e'_{x3}\cos\Phi\frac{\partial u_z}{\partial z}+(e'_{y4}\sin\Phi\cos\Phi-e'_{x5}\cos\Phi\sin\Phi)\left(\frac{\partial u_\Phi}{\partial z}+\frac{1}{r}\frac{\partial u_z}{\partial \Phi}\right)\\
&+(e'_{y4}\sin^2\Phi+e'_{x5}\cos^2\Phi)\times\left(\frac{\partial u_r}{\partial z}+\frac{\partial u_z}{\partial r}\right)+\left(-e'_{x1}\cos\Phi\frac{\sin 2\Phi}{2}\right.\\
&\left.+e'_{x2}\cos\Phi\frac{\sin 2\Phi}{2}+e'_{y6}\sin\Phi\cos 2\Phi\right)\times\left(\frac{1}{r}\frac{\partial u_r}{\partial \Phi}+\frac{\partial u_\Phi}{\partial r}-\frac{u_\Phi}{r}\right)
\end{aligned}
$$

where u is the displacement and the piezoelectric stress tensor $\overline{e'}$ is [38],

$$
\overline{e'}=\begin{pmatrix} e'_{x1} & e'_{x2} & e'_{x3} & 0 & e'_{x5} & 0 \\ 0 & 0 & 0 & e'_{y4} & 0 & e'_{y6} \\ e'_{z1} & e'_{z2} & e'_{z3} & 0 & e'_{z5} & 0 \end{pmatrix}
$$

Since the internal electric field in the surface depletion region of NWs has a radial direction, the radial piezoelectric polarization component (P_r) may result in an increase or decrease of the internal electric field strength. This effect can be modeled by considering an equivalent density of piezoelectric charges as given [37]:

$$
\begin{aligned}
N_{PE}=-\frac{1}{q}\Bigg[&(e'_{x1}\cos^3\Phi+e'_{x2}\cos\Phi\sin^2\Phi+e'_{y6}\sin\Phi\sin 2\Phi)\frac{\partial^2 u_r}{\partial r^2}\\
&+(e'_{x1}\cos\Phi\sin^2\Phi+e'_{x2}\cos^3\Phi-e'_{y6}\sin\Phi\sin 2\Phi)\\
&\times\left(-\frac{u_r}{r^2}+\frac{\partial u_r}{\partial r}\frac{1}{r}-\frac{1}{r^2}\frac{\partial u_r}{\partial \Phi}+\frac{1}{r}\frac{\partial^2 u_r}{\partial \Phi\partial r}\right)+e'_{x3}\cos\Phi\frac{\partial^2 u_z}{\partial z\partial r}\\
&+\left(e'_{y4}\sin\Phi\cos\Phi-e'_{x5}\cos\Phi\sin\Phi\right)\left(\frac{\partial^2 u_\Phi}{\partial z\partial r}-\frac{1}{r^2}\frac{\partial u_z}{\partial \Phi}+\frac{1}{r}\frac{\partial^2 u_z}{\partial \Phi\partial r}\right)\\
&+\left(e'_{y4}\sin^2\Phi+e'_{x5}\cos^2\Phi\right)\times\left(\frac{\partial^2 u_r}{\partial z\partial r}+\frac{\partial^2 u_z}{\partial r^2}\right)+\left(-e'_{x1}\cos\Phi\frac{\sin 2\Phi}{2}\right.\\
&\left.+e'_{x2}\cos\Phi\frac{\sin 2\Phi}{2}+e'_{y6}\sin\Phi\cos 2\Phi\right)\\
&\times\left(-\frac{1}{r^2}\frac{\partial u_r}{\partial \Phi}+\frac{1}{r}\frac{\partial^2 u_r}{\partial \Phi\partial r}+\frac{\partial^2 u_\Phi}{\partial r^2}+\frac{u_\Phi}{r^2}-\frac{\partial u_\Phi}{\partial r}\frac{1}{r}\right)\Bigg]
\end{aligned}
\tag{3.13}
$$

Considering this equivalent charge density which will be added to the ionized impurities (donor or acceptor), the effect of piezoelectric charges in the surface depletion region of a ZnO NW can be illustrated in Fig. 3.5 which presents the surface potential of ZnO NW with a radius 60 nm in the presence of different induced piezoelectric charge densities [37].

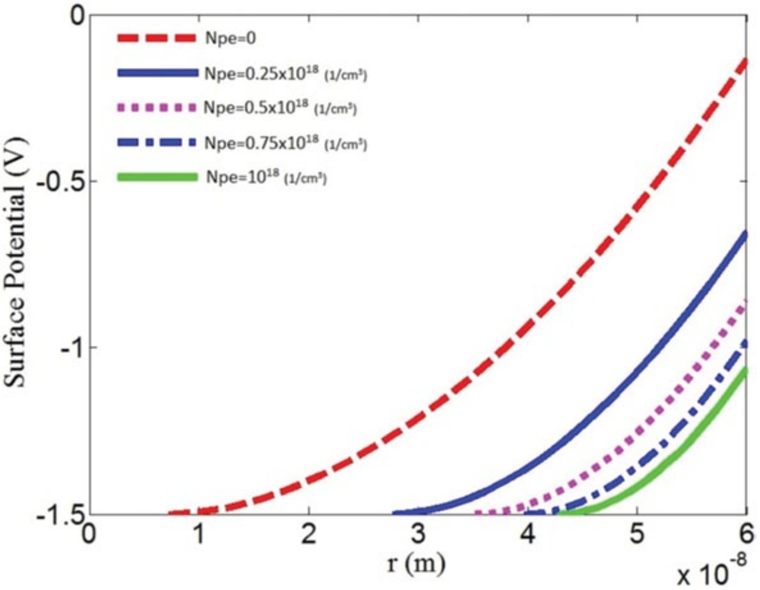

Fig. 3.5 The potential electric distribution in a ZnO NW with radius 60 nm in presence of different piezoelectric charge densities

The effect of induced piezoelectric charges on the surface potential of NWs with different radius is also depicted in Fig. 3.6. As shown the effect of piezoelectric charges on the surface potential of NWs with a smaller radius is stronger. The simulation results indicate using NWs with a small radius may increase the efficacy of NGs [37].

3.4 Design Considerations for Systems with Quantum Dots on Semiconductor Surfaces: Influence, Characterization and Applications

In many nanodevices, quantum dots (QDs) are in close proximity to semiconductor surfaces. As a means of designing such devices, the properties of these quantum-dot–semiconductor structures must be taken into account. Herein, these systems are characterized as an input to the design of nanodevices based on these systems.

Quantum dots (QDs) are nanocrystalline semiconductor materials whose size varies on the order of a few nanometers to a few hundred nanometers. They constitute a class of material having properties between the bulk and the molecular forms of matter (quantum dots) [39] These QDs exhibits discrete size dependent energy levels where electrons are confined with respect to motion in all three dimensions. By tuning the size and the composition of the QDs, light wavelengths from the

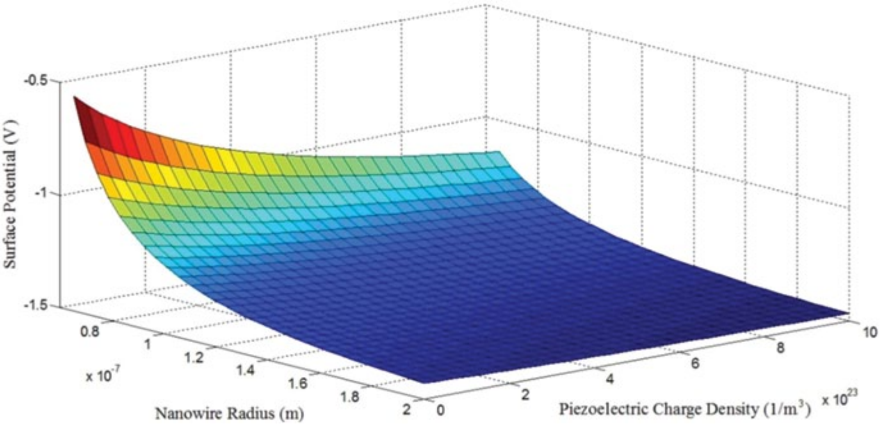

Fig. 3.6 The surface potential of a ZnO NWs with different radii as a function of of piezoelectric charges

ultraviolet to the infrared range can be achieved [40]. The wavelength of emission bands is dependent on the particle size, temperature and its distribution [41]. Because of their unique optical and physical properties, they have variety of applications in, semiconductor lasers [42–44], biomedical imaging [45, 46], optoelectronic devices [47, 48], photovoltaic and solarcells [49].

3.4.1 Core Shell Quantum Dots

Compared to plain core quantum dots (QDs), core/shell QDs offer an enhanced stability and tunability of the optical and electronic properties [50]. These core/shell quantum dots consisting of one material buried in another material with a larger band gap have received much attention due to their ability to improve the photoluminescence quantum yields by passivating surface nonradiative recombination sites [51]. The purpose of the shell material is to passivate surface trap sites and to energetically confine the electron and hole. Compared to the organically passivated dots, these coreshell structures poses higher tolerance to processing conditions that are required for integrating into solid state structures and thus more useful for optoelectronic devices [51]. Some of the examples of core-shell quantum dot structures reported earlier includes CdSe/ZnS [52], ZnSe/CdSe [53], PbSe/CdSe [41], CdS/CdSe [54], ZnS/CdS [55].

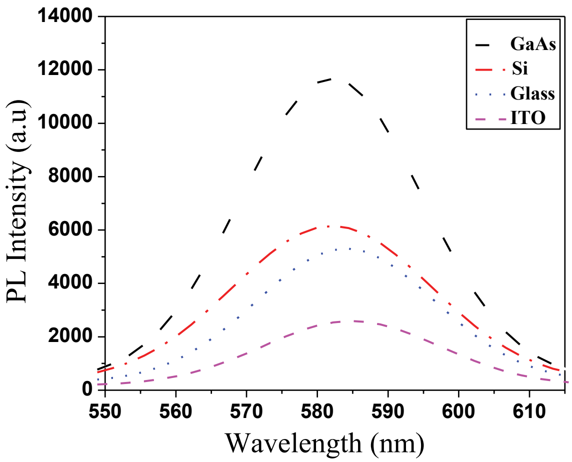

Fig. 3.7 Photoluminescence spectra of CdSe/ZnS quantum dots on GaAs, Si, Glass and ITO substrates

3.4.2 Quantum Dots on Semiconductor Surfaces

Due to the high surface to volume ratio, energy relaxation and recombination dynamics in QDs strongly depend on surface passivation conditions [56]. Not much of the work has been done to investigate the effects of quantum dots on surfaces of different substrates. Also the study of heterojunctions formed between the deposited material and substrate is highly motivated due to their applications in varied fields for example InAs QDs grown on Si substrate with good luminescence will benefit the integration of Si electronics with high-speed, low-power optoelectronic functions and permits the fabrication of large-scale optoelectronic integrated circuits [57].

In case of CdSe/ZnS core/shell QDs the fast initial relaxation dynamics has been usually explained in terms of carrier trapping at the interface (or surface related) defect states. However the origin of these states is not understood yet. Thus the optical as well as the interface state study in CdSe/ZnS core-shell QDs needs to be done and is under investigation.

a- Luminescence properties of Quantum Dots and Zinc Oxide nanowires on Surfaces of Different Substrates For getting an insight on the behavior of QDs deposited on semiconductor surfaces, CdSe/ZnS core/shell QDs is deposited on the surfaces of different substrates such as Gallium Arsenide (GaAs), Silicon (Si), glass and Indium tin oxide (ITO). In order to explore the effects of substrates on the optical properties of these quantum dots, photoluminescence (PL) measurements using a continuous wave He-Cd laser having an excitation wavelength of 325 nm. The room temperature PL spectra of CdSe/ZnS quantum deposited on the GaAs, Si, Glass and ITO coated glass are shown in Fig. 3.7. As it is seen for all the samples, the PL spectra have a peak value at a wavelength of about 582 nm with different PL intensities. Quantum dots deposited on the GaAs have the highest PL intensity and quantum dots on the ITO coated glass shows the lowest intensity [58].

Fig. 3.8 Photoluminescence spectra of ZnO nanowires on different substrate

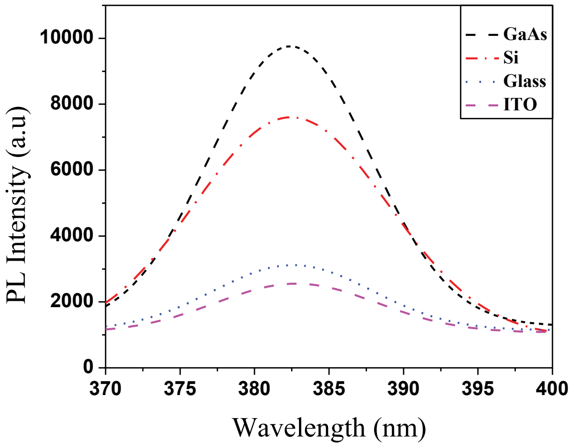

For more investigation the experiment was repeated by replacing the CdSe/ZnS quantum dots with the as grown ZnO NWs. ZnO nanowires were grown by the vapor liquid solid (VLS) method inside a horizontal quartz tube at atmospheric pressure at a growth temperature of 900–910 °C with a constant flow (350 sccm) of Ar for 30–50 min with a source consisting of zinc oxide powder mixed with graphite in a weight ratio of 1:1 with Au deposited as a catalyst. After the growth process, ZnO NWs were drop casted on the same substrates that were used for analyzing quantum dots surface properties that are GaAs, Si, ITO and glass. Figure 3.8 represent the PL spectra of ZnO NWs on GaAs, Si, ITO and glass.

The experimental results indicates that the PL intensities order for ZnO NWs deposited on substrates are similar to the PL intensities order for CdSe/ZnS quantum dots on the same substrates. This results shows that the degree of PL intensities of both samples, deposited with quantum dots and NWs, is dependent on the type of substrate being used and not on the material being deposited on them [58].

b- Heterojunction effects It has also been shown that the PL intensities order variations are not a function of the contact formed between the deposited material and the substrates. This was investigated by doing analysis at the junctions of the ZnO and ITO, GaAs and glass substrates and drawing energy band profiles for each material as shown in Fig. 3.9.

The comparison of energy barriers at the interface of junctions shows that the energy barrier seen by electrons at the interface of ITO and ZnO is minimum showing a negative energy barrier value, while the energy barrier between glass and ZnO is the highest, which is in contradictory with the experimental results. The heterojunction analysis indicates that the observed PL intensities differences is not a function of the contact formed between the deposited material and the substrates and electron transferring from substrate to the conduction band of ZnO NW cannot be responsible for the observed PL intensity difference.

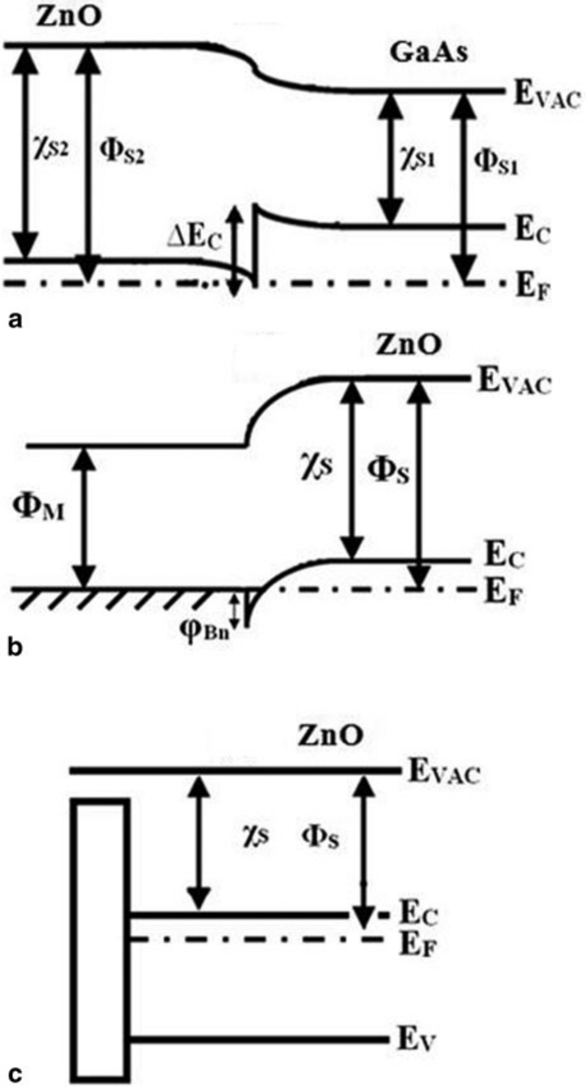

Fig. 3.9 (**a**) Energy band diagram of ZnO-GaAs heterojunction, where φ_{s1} and χ_{s1} be the work function and electron affinity of GaAs and φ_{s2} and χ_{s2} be the work function and electron affinity of ZnO respectively. (**b**) Energy band diagram of ZnO-ITO heterojunction, where χ_s is the electron affinity of ZnO; φ_s be the work function of ZnO and φ_m-work function of ITO. (**c**) Energy band diagram of ZnO-glass heterojunction, where φ_s and χ_s be the work function and electron affinity of ZnO respectively

3.4.3 Biological Applications of Quantum Dots as Mode for Designing Devices

Microcrystalline and nanostructured semiconductors are promising materials for different technological and biological applications such as quantum dots that are rapidly being applied to many emerging and existing technologies. These applications arise from their unique properties, such as tunable emission spectra, high brightness, simultaneous detection of multiple signals and long-term stability. Also the crystalline quantum dots are useful in biomedical applications because they glow brightly in different colors (depending upon their atomic structure and size) and offer valuable applications in image-guided surgery and light-activated therapies, as well as highly sensitive diagnostic tests. Compared to core type quantum dots, the core-shell type nanoparticles are more desirable for biological applications as the core being passivated by the shell that improves fluorescent properties and prevents leaching [40]. Not only in the bioimaging, these quantum dots are also used in the in solar cell construction, LEDs, and even quantum computing. Some of the major biological applications of these quantum dots are discussed in the following section.

a- Cancer Diagnostic and Therapeutic Applications Bioconjugated QDs can be used to identify potential molecular biomarkers for cancer diagnosis, treatment and prognosis. They may allow the surgeon to map sentinel lymph nodes and perform a complete surgical resection. Their unique optical properties make them ideal donors of fluorescence resonance energy transfer (FRET) and photodynamic therapy studies. Multifunctional QDs have become effective materials for synchronous cancer diagnosis, targeting and treatment [40, 59, 60]. Serum assay is most commonly used for detection of prostate cancer besides other detection probes like protein, specific DNA, mRNA sequences [61] but cancer diagnostic from serum samples only can only be possible through specific biomarker probes for which quantum dots not only serves as biosensitive probes but also used for the detection of thousands of molecules simultaneously [62].

b- Fluorescence probes for cellular proteins Quantum dots have been readily adopted by the bioscience community as fluorescence probes for biomolecular applications because of their unique optical properties, broad absorption, narrow emission spectra, high quantum yields and photostability [63, 64]. These QDs can be used as fluorescence probes for labeling cellular proteins where preservation of enzyme activity is desirable [65]. QDs that were coated with Streptavidin were used to label individual isolated biotinylated F-actin fibers. However, compared with Alexa488 (an organic fluorophore), a smaller proportion of labeled filaments were motile and intracellular labeling of these filaments has also been shown to be possible [66]. QDs have also been used to label mortalin, and p-glycoprotein, molecules that are important in tumor cells [67, 68]. Labeling with QDs was much more photostable than with organic dyes, with a 420-fold increase over the organic fluorophore. Also the photostability and advantageous signal-to-noise ratio achievable with QDs proves that they could be ideal probes for single molecule tracking studies [69].

c- Multiplexed biological detection and imaging Colloidal QDs possess excellent fluorescence properties including high emission quantum yields at room temperature and tunable emission wavelength [70]. Bioconjugated QDs have been used in DNA hybridization [71], immunoassay [72], receptor-mediated endocytosis [71], and time-gated fluorescence imaging of tissue sections [73]. Nanocrystals are also emerging as a new class of fluorescent labels for in vivo cellular imaging. An important advantage is that the extremely high photostability of QDs allows real-time

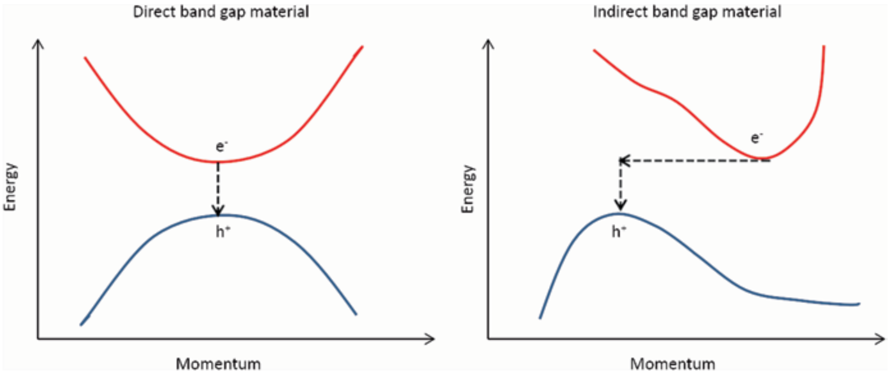

Fig. 3.10 Relative energies and momenta of valence (*blue*) and conduction (*red*) bands in direct band gap (*left*) and indirect band gap (*right*) materials

monitoring or tracking of intracellular processes over long periods of time. Another advantage is the ability to use multicolor nanocrystals to simultaneously image multiple targets inside living cells or on the cell surface. Furthermore, with an inert layer of surface coating, the nanocrystals are believed to be less toxic than organic dyes. Also conjugated luminescent QDs is used to transfer an iron transport protein antibodies that recognize cancer biomarkers, and folic acid (a small vitamin molecule recognized by many cancer cells). In each case, it was found that receptor-mediated endocytosis occurred and the nanocrystals were transported into the cell [74].

3.5 Nanodevices for DNA Cleaving

Herein, design considerations are presented that enable the fabrication of nanodevices that undergo photo-production of electron/hole pairs in indirect bandgap semiconductors; as will be discussed the holes produced in this process can be filled by electrons from an electron-rich DNA molecule bound to the indirect bandgap semiconductor. The physics underlying the design of these nanodevices for cleaving DNA sheds light in important design consideration for the nanodevices.

In semiconductors, recombination can occur if both energy and momentum are conserved.

After the generation of an electron/hole pair, recombination can occur if both energy and momentum are conserved as illustrated in Fig. 3.10. This is easily achieved in a direct band gap material because the electrons and holes possess the same momentum, and the energy difference resulting from the recombination is released in the form of a photon. In an indirect band gap material, however, the electron and hole momenta differ, making it necessary for the electron to participate in a momentum-chasnging process before recombining. Because recombination is less favorable in indirect band gap materials, they are often used to generate current flow.

TiO_2 has an indirect band gap of 3.2 eV [75]. When exposed to light of energy greater than the band gap, electon/hole pairs are formed, which then have the potential to oxidize surrounding species. If the oxidation potential of the TIO_2/dopamine is more positive than the redox properties of the attached DNA, which is generally the case, the holes are transferred to the DNA from TiO_2 [75, 76]; dopamine is used as a surfactant since it has energy level that facilitate charge transfer as discussed in Ref. 76. This charge transfer was determined to occur via multi-step hopping, where a charge is propelled from one base to the next via thermal fluctuations [77, 78]. Accumulation of holes in one location can results in DNA cleavage. Out of the four DNA nucleosides, guanosine has redox potential most conducive to hole transfer, and, consequently, it was found that guanine (G) undergoes hydroxylation in DNA-TiO_2 complexes after exposure to light [79]. Kanvah et al. studied the cleavage of DNA bound to anthraquinone derivative (AQ) photosynthesizer, which functions similarly to TiO_2 in that it modifies DNA bases to their radical cation form upon exposure to light. It was confirmed that the reaction most frequently occurs at guanine, resulting in its conversion to 8-oxo-7,8-dihydroguanine. In addition, adjacent guanines have a lower relative potential energy than isolated guanines. This means that holes are more likely to accumulate in and cleave at regions of DNA with several adjacent guanines. A correlation also exists between the likelihood of cleavage and distance from the particle where the electron/hole pairs are generated. GG sites closest to AQ react and cleave at a much higher rate than those further away. The hopping model of charge transfer attributes this phenomenon to the rate constant for reversible hopping (k_{hop}) and the rate constant for irreversible trapping (k_{trap}). When $k_{hop} > k_{trap}$, all trapping sites in the sequence have an equal probability of reaction. When $k_{hop} < k_{trap}$, the reaction is more likely to occur closer to the site of initial oxidation. The surrounding bases also influence the reactivity of guanines; it has been shown that adjacent cytoxine (C), thymine (T) and, in the case of RNA, uracil (U), all decrease the reactivity of G [78].

Using this information, one can create a nanocomposite for cleaving DNA [80, 81]. In Paunesku et al., TiO_2 particles 4.5 nm in diameter were created by first synthesizing TiO_2 colloids via dropwise addition of titanium(IV) tetrachloride to cooled water. Oxygen was removed by bubbling with nitrogen, and the particles were suspended in glycidyl isopropyl ether. This provides a coating for TiO_2 and prevents unwanted reactions between hydroxyl groups on the TiO_2 with phosphodiester groups on the DNA oligonucleotides. The nucleotides were synthesized with a carboxyl group on the 5′ end, which was then used to bind to an amine group on a dopamine molecule. When exposed to TiO_2, the dopamine replaces glycidyl isopropyl ether coating the TiO_2 particles, resulting in the binding of TiO_2 to DNA via dopamine. The ratios used were such that there were approximately 50 DNA molecules per TiO_2 particles. The oligonucleotides were then hybridized to complimentary strands to obtain double stranded DNA bound to TIO_2. Vasudev et al. confirmed that binding in achieved by performing Raman spectroscopy measurements on the resulting compounds. The spectra contained characteristic DNA peaks in the 800–1,500 cm^{-1} range, as well as a TiO_2 peak around 190 cm^{-1} ([82], Fig. 3.11).

Paunesku et al. demonstrated that these nanocomposites can be used to cleave DNA at the guanine sites. Gel electrophoresis analysis of the nanocomposites after 0, 8 and 10 min of UV light exposure indicated a higher percentage of cleaved DNA for longer exposure times [80]. UV light also causes cleavage at G-rich sites

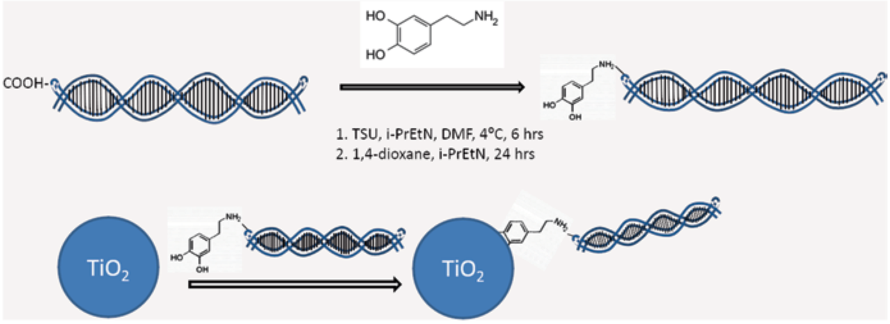

Fig. 3.11 Synthesis of DNA-dopamine-TIO_2 nanocomposites. Diagram not to scale

in TiO_2-DNA composites with three DNA strands that form a T-shaped three-way junction [83, 84].

3.6 SERS Nanosensors

Surface-enhanced Raman spectroscopy can be used to determine the biological composition of a sample by detecting the unique vibrational signature of specific molecules. In order to obtain these vibrational signatures, a nanosensor needs to be designed [85].

An example of a nanosensor is Apt-$\alpha_V\beta_3$ adsorbed to a silver nanorod (AgNR) SERS substrate [86]. Apt-$\alpha_V\beta_3$ is a 85-base long RNA molecule generated for binding to a cellular membrane protein called $\alpha_V\beta_3$ integrin. This integrin normally interacts with the RGDV peptide, a process which is amplified in cancerous cells. By binding to this integrin, Apt-$\alpha_V\beta_3$ blocks the binding site, possibly hindering cancer progression [87]. Obtaining the Raman spectrum of this potentially useful molecule would help in its further studies.

Apt-$\alpha_V\beta_3$ (exact 5′ to 3′ sequence: GGGAGACAAGAAUAAACGCUCAAUUCAACGCUGUGAAGGGCUUAUACGAGCGGAUUACCCUUCGACAGGAGGCUCACAAACAGGC) with an amine modifier at the 5′ end was suspended in water and placed on a patterned multiwall AgNR SERS chip [88] in nitrogen for 24 h. The substrate was then washed, removing the access RNA and leaving only the RNA adsorbed to the nanorods. The SER spectrum obtained with a 514 nm laser contained peaks consistent with previously-published spectra of DNA and RNA bases [85, 89–91]. In addition, the substrate enhanced the signal by as much as 58 times compared to standard microRaman [86], demonstrating the effectiveness of the AgNR substrate in nanosensor design.

3.7 Design of Nanowire Polarizers

Recent progress in the synthesis of semiconductor nanowires has enabled the testing of quantum confinement effects and developing nanodevices based on these materials. However, isolating and manipulating the free-standing tangled nanowires still remains a challenges. Great interest has been shown in research focused on growing nanowires on a substrate in a controlled fashion, so that little or no post-processing device applications. The polarization anisotropy can be explained in terms of the large dielectric difference between these freestanding nanowires and surrounding environment. This property of polarization anisotropy is considered here as it relates to polarization sensitive nanoscale photodetectors that can be useful in integrated photonic circuits, optical switches and interconnects, near-field imaging, and high resolution detectors [92].

Before considering the theory underlying the design of such nanowire polarizers, it is instructive to consider relevant details of the fabrication process. In order to achieve free standing nanowires, large periodic arrays of semiconductor nanoporous structure needs to be fabricated that will allow (i) the size and composition to be varied, (ii) flexibility to use a variety of substrate materials, and (iii) compatibility with various fabrication processes. Porous alumina templates have the best attributes for growing uniform pores of nanowires or nanotubes due to their high aspect ratio. They are durable and can withstand high temperatures (up to 800 or 1,000 °C) [94, 97]. The length and diameter of the pores can also be controlled by changing the experimental conditions [93–97].

Advantages of using an insulating alumina matrix is that it allows us to (i) easy to perform annealing treatments without losing nanocrystallinity, and (ii) study a single nanoscale heterojunction inside the pores. With such a template we have (i) uniform regular distribution of nanopores of the order of a few nanometers, (ii) arrangement of vertically directed pores with high aspect ratio, (iii) ability to control diameter of cells and pores by changing electrolyte composition and electrochemical processing parameters, and (iv) high reproducibility of the film structure.

Confinement of materials like CdS nanowires inside these templates have a unique advantage of increased band gap energy due to quantum confinement. Thus making nano-structured CdS a better window material than bulk CdS [98]. Hence, the alumina matrix is the best template for growing free standing nanowires and the alumina template can be dissolved leaving behind only the nanowires.

3.7.1 Theoretical Model

The polarization anisotropy in PL measurements between the free standing nanowires and its surrounding environment can be modeled by treating the nanowire as an infinite dielectric cylinder in a vacuum, since the wavelength of the exciting light is much greater than the wire diameter. When the incident field is polarized parallel to the cylinder, the electric field inside the cylinder is not reduced. But when polarized perpendicular to the cylinder, the electric field amplitude is attenuated according to

$$E_i = \frac{2\varepsilon_0}{\varepsilon + \varepsilon_0} E_e \tag{3.14}$$

where E_i is the electric field inside the cylinder, E_e the excitation field, and ε_0 is the dielectric constant of the cylinder (vacuum) (100) and ε is the dielectric constant of the surrounding material. For $\varepsilon > \varepsilon_0$, the probability of optical transitions in a nanowire depend on light polarization, acquiring maximal values for light with polarization parallel to the nanowire axis whereas illuminating with unpolarized light creates a high frequency electric field in the nanowire in the direction of polarization parallel to the nanowire axis. These polarizations exhibit a strong dependence on the absorption coefficient, *k*, both inter- and intraband, on the light polarization for a system of parallel wires. The ratio of absorption coefficient, *k*, for the two light polarizations is given by the Eq. (3.15)

$$\frac{k \,||}{k \perp} = \left(\frac{\varepsilon + \varepsilon_0}{2\,\varepsilon_0} \right)^2 \tag{3.15}$$

This absorption coefficient, k, ratio is more than 30 for free standing nanowires having air with $\varepsilon_0 = 1$ otherwise, it is 4.7 for nanowires in an Al_2O_3 matrix which has $\varepsilon_0 = 3$ [100]. Due to the dielectric constant difference between the nanowires and their surrounding, huge polarization anisotropy is manifested in photoluminescence (PL) measurements. The PL spectra [101] can be recorded from a number of individual wires as a function of excitation or emission polarization [1]. On average, the excitation and emission polarization ratio is given by equation:

$$\rho = \frac{I \,|| - I \perp}{I \,|| + I \perp} \tag{3.16}$$

with the intensities parallel $(I_{||})$ and perpendicular $(I_{\perp})$ to the wire being measurable with PL measurements at different angles of orientation.

Polarization anisotropy in quantum wires is caused by the mixing of valence bands due to quantum confinement. This quantum mechanical effect results in smaller polarization ratios ($\rho < 0.60$) which are reported [102–104]. The large polarization response is due primarily to the large dielectric contrast between the nanowire and its air or vacuum surroundings. With the increasing excitation power density, the photoconductance (PC) of nanowires is increased in a reproducible and reversible manner with respect to the excitation power. The photoconductive response results from direct carrier collection at the nanowire–metal contact interface versus population of surface traps. The photoconductivity anisotropy ratio is given by the following equation:

$$G = \frac{G_{||} - G_{\perp}}{G_{||} + G_{\perp}} \tag{3.17}$$

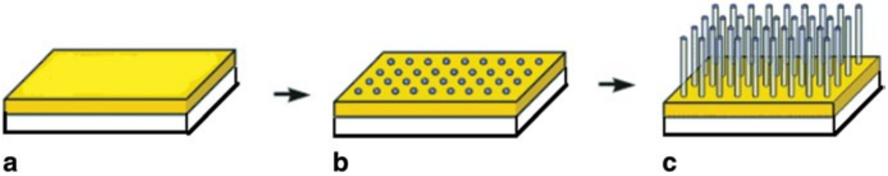

Fig. 3.12 Flowchart for the fabrication of CdS nanowires **a** 200 nm of Aluminum layer (*yellow*) deposited on ITO coated glass substrate. **b** After anodization of Al layer leading to formation of nanopores of 40–100 nm. **c** CdS nanowire array after the DC electrodeposition growth

where $G_{\parallel}$ and $G_{\perp}$ are the conductances with parallel and perpendicular excitations respectively. To summarize the nanowire is modeled as an infinite dielectric cylinder in a vacuum with the light polarizations causing the electric fields. The electric field intensities calculated from Maxwell's equations imply that the field is strongly attenuated inside the nanowire for the perpendicular polarization, $E_{\perp}$ whereas the field inside the nanowire is unaffected for the parallel polarization, $E_{\parallel}$.

3.7.2 Implementation of Design Concepts

Nanopores were produced in Anodized Aluminium Oxide (AAO) nanoporous template layer coated on ITO-coated (indium tin oxide-coated) glass using a two step anodization process in 0.3 M oxalic acid solution. The procedure for fabricating anodized aluminum oxide consists of an electro chemical cell with the aluminum substrate as anode, platinum plate (1″ × 1″) as cathode at 5 °C. The anodized substrate is then rinsed with DI water and dried in nitrogen. The grown AAO layer has pores of 40–60 nm but it also grows with a barrier layer of oxide at the interface of the Al and Al_2O_3 which can be removed by dipping the substrate in 50 % phosphoric acid (H_3PO_4) for 2–4 min.However, due to poor adhesivity of Al layer to the ITO/glass substrate, a thin layer of titanium (Ti) or titanium dioxide (TiO_2) is deposited prior to anodization. CdS nanowires are grown by DC electrodeposition. The electrolyte for CdS deposition is 0.055 M $CdCl_2$ and 0.19 M elemental sulfur, dissolved in 50 ml dimethyl sulfoxide (DMSO) at 120 °C with a constant current density supply of 7.5 mA cm^{-2} for 7 s. The estimated growth rate was 30 nm s^{-1}. The flowchart for the electrodeposition is given below in Fig. 3.12:

The bottleneck lies in growing the cadmium sulphide (CdS) nanowires in a reproducible fashion. The non uniform thickness of the aluminum oxide barrier layer leads to these problems which include: template cracking at the electrolyte/air interface during anodization, low filling ratio of nanorods/nanowires, and large variance in the length of nanorods/nanowires [105].

After the growth of CdS nanowires, the alumina matrix is usually dissolved in 1 M sodium hydroxide solution leaving behind the free standing nanowires.

For these designs, the PL and PC polarization anisotropy is expected to be nearly wavelength-independent for energies larger than the nanowire band gap. For these designs it is possible to realize devices that simultaneously measure intensity and polarization and use them as optical photodetectors [106–108]. The ability synthesize nanowires out of any group IV, III–V, or II–VI semiconductor material like InP, CdS, GaN, etc. facilitates the creation of a wide range of detectors and high-resolution detector arrays for different spectral regimes.

3.7.3 Sensing Elements on Graphene-Based and Carbon-Nanotube-Based Substrates

The design of biosensors with molecular sensing elements on graphene-based and carbon-nanotube-based substrates is sensitive to the nature of the bond between the molecular sensing element and the substrate. In particular, it is important that the binding be accomplished in a manner so as to leave the transport properties of the carbon-based substrate unaffected. Non-covalent functionalization may be accomplished effectively, as it does not create atomic scale defects, which are disruptive. Herein, the functionalization of carbon nanotubes and graphene using peptides is considered in the context of designing these nanobiosensors.

3.7.4 Peptides that Bind to Graphene

Kim et al. [109] presented findings on the preferential binding of peptides to the graphene edges and planes. The peptides EPLQLKM and HSSYWYAFNNKT have been found to preferentially bind to graphene edges and surfaces, respectively. This critically helps in defining the electronic and mechanical properties of graphene and is attributed to the π- π interactions. EPLQLKM interacts with the positively-charged hydrogen-terminated edge of the graphene through the negatively-charged glutamate residue, E, while the graphene plane binding peptide does so through π-π stacking [110] of the aromatic rings of the H-Y-W-Y-F residue [111].

Lu et al. [112] have used pyrene moiety (1-pyrenebutyric acid) attached to N-terminus of peptides to bind to graphene oxide layer to monitor protein-peptide interactions. Peptides used are pyrene-GGGRKRIHIGPGPAFYTT and pyrene-GGGNSWGCAFRQVC. Pyrene-based fluorophores re-emit light upon excitation and the number of times a specific event occurs per photon adsorbed is very high, hence making it a good choice for an optical contrast agent in molecular beacons [113, 114]. Also, pyrene reacts noncovalently with carbon nanotubes and graphene due to π bonds present [115]. Due to the proximity of graphene oxide layer to pyrene, the fluorescence of pyrene is quenched but owing to the adhesive properties of pyrene [112], when the peptide binds to the protein, there is competition between pyrene and target-protein for the graphene oxide layer, leading to desorption and dequenching of pyrene, which aids in detecting target protein.

Self-assembling peptide sequences are made use of by So et al. [116] to bind to graphene surfaces. Among the biocombinatorially selected sequences, one of the peptides—IMVTESSDYSSY, designated as wild type is used. Using AFM, the capability of the peptide to form highly ordered structures over graphite was determined and a high level of symmetric formation observed. This is likely due to the molecular recognition of the hexagonal structure of the graphite. A very high correlation was observed between the sequence of the peptide and the formation of the self-assembled structures. Also, the process of formation of a peptide over graphene involves a transition between the amorphous state to an orderly state and further analysis has shown that the aromatic, hydrophilic and hydrophobic domains of a peptide correspond to the binding ability, diffusion and the self-assembly of the peptides [116].

Katoch et al. [117] have made use of the peptide GAMHLPWHMGTL, previously known to bind to graphene [118] to observe its structure on binding. It has been observed that the peptide formed a helical structure on binding with the graphene surface and the structure was much different than that of an α-helical structure. Further, Raman spectra were analyzed to determine if incubation of the peptide had any effect on the binding but no significant difference was observed. Also, it has been shown that tryptophan is an essential amino acid required for binding to graphene [117].

3.7.5 Peptides that Bind to Carbon Nanotubes

Wang et al. [119] have used phage display technique [119] to determine one of the possible sequences of peptide that can be used to bind to carbon nanotubes. In this method, the bacteriophage is infused exteriorly with different peptide sequences and suspended in a detergent solution, in the presence of nanotubes. This mixture is then incubated for about an hour at room temperature which was then followed by centrifugation. This resulted in the elution of bound phage particles. The binding was stronger when the number of plaque forming units (PFU), a measure of binding phage concentration, was higher. To further establish the binding, phage clones were loaded onto microspheres and incubates with SWNTs. The specific peptide sequences were determined by using a single crystal graphite and one such sequence is WPHHPHAAHTIR. Also, the middle region of the peptide sequence seem to be reacting more with the nano tube than the ends and W and H seem to play an important role in stronger binding [119].

Dieckmann et al. [120] has developed reversible cyclic peptides, based on the cyclic peptides synthesized by Ghadiri and co-workers [13]. These RCPs have alternating L and D chiralities, have the ability to adopt a planar formation due to all the side chains pointing radially outward, leaving the middle open, where the SWNT is infused. The presence of open cysteine bonds instead of being introduced into the backbone, makes it easier to synthesize as well as helps in closing of the peptide, by wrapping itself around the carbon nano tube of appropriate diameter. This also prevents aggregation of CNTs in solution due to hydrophobicity [120].

Wang et al. [122] used fluorescent-labeled p21WAF-1 (cyclin-dependent kinase inhibitor 1) derived CBM peptide probe, FITC-HAKRRLIF to bind to graphene oxide, synthesized by a modified Hummers method [123] and carbon nanotubes. The interaction between the phenylalanine residue present at the end of the peptide and the α-bond shows binding between the amino acid residues and graphene, further demonstrated by the steady increasing curve of graphene in the Stern-Volmer plot [124]. This setup is used to detect Cyclin A_2, an important indicator of early-stage cancer by the process of quenching of the peptide by Graphene oxide and detection is possible at the nano scale, 10 fold better than SWNTs and 1200 fold better than the Tb^{3+} chelating macrocycle [122].

Pantarotto et al. [125] makes use of peptides binding to CNTs to devise vaccines. Fragment condensation or chemical ligation is employed in this process. While the former method involves coupling of peptide fragments and has the disadvantages of racemization and the presence of excess concentration of the coupling fragment, the latter operates through a chemoselective reaction of deprotected peptides to give rise to a unique reaction product that binds to the CNT. A pentapeptide is used in fragment condensation while a peptide isolated from a Foot and Mouth disease virus is used in chemical ligation. As confirmed by ELISA and surface plasmon resonance test, the FMDV peptide retained its antigenic properties. Characterization of the peptide bound was performed by TEM and NMR spectroscopy. Thus, this paper discusses that the peptide isolated from the FMDV virus induces an immune response that can be made use of by making vaccines [125].

Huan et al. [126] make use of a Multi Walled Carbon Nanotube with a sensing layer of polyalinine, a polymer with high electrical conductivity, to bind to a peptide sequence of HKHAHNYRLPASGGKK, a peptide sensitive to Antharax protective antigen (PA) [127]. Detection was possible at concentrations as low as 0.4 pM. The polyalanine was formed on glassy carbon electrode using cyclic voltammetry while the MWCNT is modified to have a COCl group by suspending in HNO_3 and $SOCl_2$. This COCl group helps in binding with the peptide by forming a CON bond, releasing HCl. Square wave voltammograms (SWVs) of peptide immobilized MWCNT-PANI with different concentrations of PA ranging from 20–100 pM were collected. The sensitivity, correlation coefficient, sensing area and limit of detection were measured for every different concentration using regression analysis, selectivity was measured by observing the SWVs of a mixture of Bovine Serum Albumin (BSA) and PA and the longevity of the sensor was measured over a span of 6 days, with a signal drop of 60 % on the sixth day. High sensitivity and electrochemical signal of this sensor shows good promise in devising similar sensors for a wide range of diseases by using peptides that bind to disease-specific markers.

Mirzaei et al. [128] demonstrated that peptides that bind to carbon nanotubes have specific configurations and preferences, based on various parameters obtained from Density Functional Theory (DFT) calculations. Different models of (5,0) zigzag CNTs functionalized with a $(Me)_2CONH$ peptide through the tip or sidewall were assessed. The most favorable structure, determined from binding energy values was observed when the nitrogen of the peptide group attached to the tip of the CNT while the bonding environment of the carbonyl carbon was kept unaltered. Another parameter, the quadrupole coupling constant (C_Q), was evaluated at the oxygen and nitrogen sites of the peptide bond and significant decrease in their values was observed when compared with their original values which possibly suggests that electrons are shared between these atoms and the CNTs, critical for the bridging property of the peptide with other molecules.

3.8 Design Considerations for SERS-based Nanosensors for Biomolecules

The use of surface-enhanced Raman scattering (SERS) in the design of nanosensors present unique features in terms of designing the nanosensors for optimum performance. Herein, the basic properties of such SERS-based nanosensors are considered as the basis for optimizing the design of these nanosensors.

Surface-enhanced Raman scattering (SERS) is a phenomenon used to enhance the signal produced by Raman scattering. Raman spectroscopy is a useful tool for sensor development with potential for remote sensing. Raman spectra provide information on the vibrational modes or phonons, between and within molecules. Therefore, you can produce a unique spectral fingerprint for single molecules. SERS is accomplished through the use of substrates with nanometer scale geometries made of metals with many free electrons, such as silver, gold, or copper. Silver is the best choice for frequencies in the visible range and has the lowest damping rate when compared to Au, Cu, and Al [129]. These metals produce surface plasmons, which are oscillating electrons, when excited with a laser. The predominant theory on why SERS causes large enhancements of Raman signals is mainly explained by the electromagnetic properties of nanostructures [130]. The strong localized surface plasmons produced on the surface of the metal by laser excitation enhance the Raman scattering of the molecule near the metal surface. This enhancement is important because Raman cross sections are between 10^{-31} and 10^{-29} cm^2/molecule, compared to fluorescence cross sections which are up to 10^{-16} cm^2/molecule. Furthermore, the Raman signal is proportional to the Raman cross section, the excitation laser intensity, and the number of molecules in the field of detection. Therefore, by enhancing the signal via SERS, fewer molecules are required for a sufficient signal to be produced.

From Pre-lim: Progress in the use of SERS is illustrated by the fabrication of SERS substrates using silver [131–133]. Moreover, SERS has been considered as a possible basis for chemical and biological nanosensors [134]. Furthermore, the fundamental role played by plasmons in the SERS process has been considered by a number of authors including Ref. [135]. Techniques for enhancing Raman signals through substrate fabrication include: (a) nanosphere lithography to produce a silver film over nanospheres (AgFON)(Van Duyne ref and milana's paper) [136], (b) silver nanorod (AgNR) arrays fabricated with the Oblique Angle Deposition (OAD) technique at University of Georgia—Athens [131] and used to detect trace levels of viruses by Shanmukh et al. 2006 [137], (c) optical antennas

[138], (d) metal doped sol-gels [139], and (e) gold core with silver shell nanoparticles [140, 141].

AgNR arrays produce enhancement factors of 10^8 without the formation of "hot-spots" [131] Chen et al. showed how an array of silver nanoparticles or AgFON, has much greater enhancement where defects occur in the array (10^8 compared with 10^4), but these spaces only account for 0.3 % of the excited area [136]. The more homogenous surface of the AgNR substrate in terms of enhancement, allows for a more reproducible substrate to be fabricated. Oblique angle deposition is a physical method using a modified E-beam evaporation system. The substrate was created by first applying a titanium adhesion layer, followed by a 200 nm Ag-film base layer onto a glass slide. In order to form silver nanorods, the substrate was positioned such that it formed an oblique angle (4°) relative to the incident vapor. This caused the surface normal of the substrate to be almost parallel with the incident vapor direction. While in this arrangement 2,000 nm of Ag was deposited to produce the nanorod array. This process allows for the length and diameter of the nanorods to be controlled, which in turn means the aspect ratio of the nanorods is controlled. A higher aspect ratio will produce a stronger enhancement effect [131, 142]. The enhancement factor is also influenced by the lateral arrangement of the nanorods. The more overlap there was between nanorods, the greater the SERS signal [131, 142, 143]. This distance dependent effect, due to the coupling of surface plasmons between nearest-neighbor nanorods, has also been shown with Ag nanoparticles by Schatz et al. [144].

Brenneman et al. used the AgNR array substrates for the detection of single stranded DNA sequences with a Renishaw microRaman system with an Ar^+-ion laser (514.5 nm wavelength) [145]. Figure 3.13 shows the spectrum obtained for a sequence of 15 thymine bases. A solution of the DNA was applied to the substrate and allowed to incubate overnight to allow adsorption of the target to the nanorods. The substrate was then rinsed with Milli-Q water to leave only a monolayer for analysis. This spectrum illustrates modes that are characteristic of thymine oligonucelotides, including multiple ring breathing modes at 610, 788, 1,007, and 1,230 cm^{-1} [146]. The sharp peak at 1,293 cm^{-1} was attributed to ring distortion and anti-symmetric bending of N3-H and C6-H [147]. A vibration form the sugar-phosphate backbone was also identified at 1,184 cm^{-1}. In addition to the detection of thymine, the vibrational modes also provide information regarding the adsorption of the molecule to the substrate. The presence of a line for stretching of the single bond C2-O (1,331 cm^{-1}) coupled with the absence of a line for the double bond C2 = O indicates that thymine is adsorbing to the nanorods through that atom.

A second sequence, known as the thrombin binding aptamer (TBA), was also evaluated using the AgNR SERS substrate. The TBA contains thymine and guanine bases and the SERS fingerprint is below in Fig. 3.14. There are several peaks attributed to guanine that are not scene in the poly-thymine spectrum. The TBA sample has a sharp peak at 805 cm^{-1}, which has been shown to be a SERS mode for guanine [89]. The SERS spectra collected for these two different sequences using AgNR arrays demonstrate how a spectral fingerprint can be used to distinguish between samples. It could also identify or detect targets with known SERS signatures.

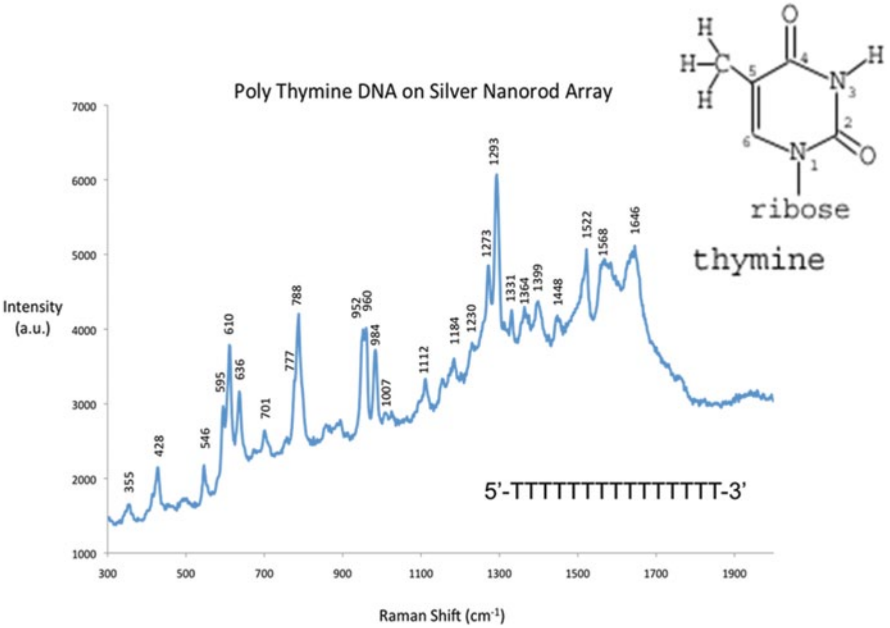

Fig. 3.13 SERS spectrum of single stranded poly-thymine oligonucleotides on AgNR array. *Upper left* is thymine and the ribose sugar and phosphate group, which comprise the DNA backbone

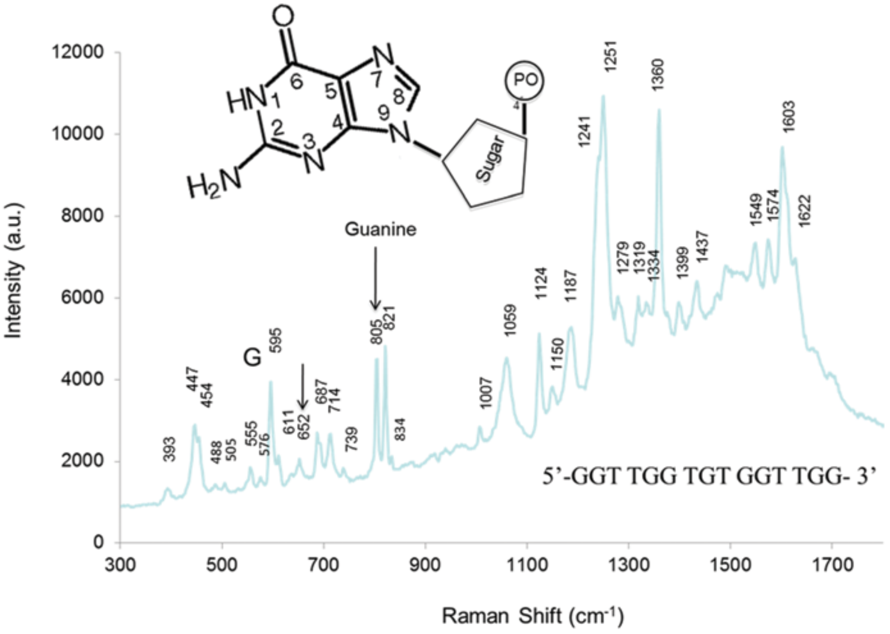

Fig. 3.14 SERS spectrum of DNA sequence TBA. *Upper left* is the base guanine. *Arrows* indicate peaks associated with the base guanine

Biosensing can be accomplished using Raman spectroscopy through the use of SERS substrates like the AgNR arrays fabricated with the oblique angle deposition technique discussed above. Moreover, it can be done using very low sample concentrations, which is useful in biomedical applications where samples can be expensive as well as in detecting harmful toxins.

References

1. Robertson DL, Joyce GF (1990) Nature 344:467–468
2. Tuerk C, Lold G (1990) Science 249:505–510
3. Ellington AD, Szostak JW (1990) Nature 346:818–822
4. O'Sullivan CK (2002) Anal Bioanal Chem 372:44–48
5. Kleinjung F, Klussmann S, Erdmann VA, Scheller FW, Furste JP, Bier FF (1998) Anal Chem 70:328–331
6. Yamamoto R, Baba T, Kumar PK (2000) Genes Cells 5:389–396
7. Fang X, Sen A, Vicens M, Tan W (2003) ChemBioChem 4:829–834
8. Xiao Y, Lubin A, Heeger A, Plaxco K (2005) Angew Chem Int Ed Engl 44:5456–5459
9. Lai R, Plaxco K, Hegger A (2007) Anal Chem 79:229–233
10. Radi AE, Acero Sánchez JL, Baldrich E, O'Sullivan CK (2006) J Am Chem Soc 128:117–124
11. Xiao Y, Piorek BD, Plaxco KW, Heeger AJ (2005) J Am Chem Soc 127:17990–17991
12. Geim AK, Novoselov KS (2007) Nat Mater 6:183–191
13. Chen JH, Jang C, Xiao S, Ishigami M, Fuhrer MS (2008) Nat Nano 3:206–209
14. Peres NMR, Castro Neto AH, Guinea F (2006) Phys Rev B 73:195411
15. Ando T, Nakanishi T, Saito R (1998) J Phy Soc Jap 67:2857–2862
16. Standley B, Bao W, Zhang H, Bruck J, Lau CN, Bockrath M (2008) Nano Lett 8:3345–3349
17. Wallace PR (1947) Phys Rev 71:622
18. Xu K, Erricolo D, Dutta M, Stroscio M (2012) Superlattice Microstruct 51:606–612
19. Xu K, Qian J, Shukla P, Dutta M, Stroscio MA (2012) 15th International Workshop on Computational Electronics(IWCE). doi:10.1109/IWCE.2012.6242868
20. Bourianoff G, Brillouet M, Cavin RK, Hiramoto T, Hutchby JA, Ionescu AM, Uchida K (2010) IEEE Proc 98:1986–92
21. Cui Y, Wei Q, Park H, Lieber CM (2001) Science 293:1289–1292
22. Kong J, Franklin NR, Zhou C, Chapline MG, Peng S, Cho K, Dai H (2000) Science 287:622–625
23. So HM, Won K, Kim YH, Kim BK, Ryu BH, Na PS, Kim H, Lee JO (2005) J Am Chem Soc 127:11906
24. Huang Y, Dong X, Shi Y, Li CM, Li L, Chen P (2010) Nanoscale 2:1485–1488
25. La Van DA, McGuire T, Langer R (2003) Small-scale systems for in vivo drug delivery. Nat Biotechnol 21(10):1184–1191
26. Calhoun B, Daly D, Verma N, Finchelstein D, Wentzloff D, Wang A, Cho S-H, Chandrakasan A (2005) Design considerations for ultra-low energy wireless microsensor nodes. IEEE Trans Comput 54(6):727–740
27. Flatscher M, Dielacher M, Herndl T, Lentsch T, Matischek R, Prainsack J, Pribyl W, Theuss H, Weber W (2010) A bulk acoustic wave (BAW) based transceiver for an in-tire-pressure monitoring sensor node. IEEE J Solid-State Circuits 45(1):167–177
28. Guyomar D, Lallart M (2011) Recent progress in piezoelectric conversion and energy harvesting using nonlinear electronic interfaces and issues in small scale implementation. Micromachines 2:274–294
29. Zhu G, Yang R, Wang S, Lin Wang Z (2010) Flexible high-output nanogenerator based on lateral ZnO nanowire array. J Nano Lett 10:3151–3155

30. Aktakka EE, Peterson RL, Khalil Najafi (2011) A self-supplied inertial piezoelectric energy harvester with power-management IC. ISSCC
31. Wang ZL, Song J (2006) Piezoelectric nanogenerators based on zinc oxide nanowire arrays. Science 312(5771):242–246
32. Hickernell FS (2005) The piezoelectric semiconductor and acoustoelectronic device development in the sixties. IEEE Trans Ultrason Ferroelectr Freq Control 52:737–745
33. Alexe M, Senz S, Schubert MA, Hesse D, Gosele U (2008) Energy harvesting using nanowires? Adv Mater 20:4021–4026
34. Auld BA (1973) Acoustic fields and waves in solids. Wiley, New York
35. Withers RS (1984) Electron devices on piezoelectric semiconductors: a device model. IEEE Trans Sonic Ultrason 31:117–123
36. Li M, Xing G, Foong Nien Ah Qune L, Xing G, Wu T, Hon Alfred Huan C, Zhang X, Sum TC (2012) Tailoring the charge carrier dynamic in ZnO nanowires: the role of surface hole/electron traps. Phys Chem Chem Phys 14:3075–3082
37. Purahmad M, Stroscio MA, Dutta M (2013) A theoretical study on the effect of piezoelectric charges on the surface potential and surface depletion region of ZnO nanowires. IOP J Semicond Sci Technol 18(1):015019 (6 pp)
38. Sen B, Stroscio M, Dutta M (2011) Piezoelectricity in wurtzite polar semiconductor nanowires: a theoretical study. J App Phys 110:024506
39. Brus L (1991) Quantum crystallites and nonlinear optics. Appl Phys A 53:465–474
40. Wang J, Han S, Ke D, Wang R (2012) Semiconductor quantum dots surface modification for potential cancer diagnostic and therapeutic applications. J Nanomater 2012(129041):1–8
41. Reiss P, Protie`re M, Li L (2009) Core/shell semiconductor nanocrystals. Wiley-inter Sci 2:154–168
42. Dutta M, Stroscio MA (2000) Advances in semiconductor lasers and applications to optoelectronics. World Sci 16:235–240
43. Koroknay E, Schulz W-M, Eichfelder M, Roßbach R, Jetter M, Michler P (2010) InP quantum dots for applications in laser devices and future solid-state quantum gates. J Phys 245:012077
44. Stroscio MA, Dutta M (2004) Biological nanostructures and applications of nanostructures in biology. Bioelectr Eng 2
45. Alexson D et al (2005) Semiconductor nanostructures in biological applications. J Phys: Condens Matter 17:26
46. Lembrikov BI, Ben-Ezra Y (2005) Quantum dot-in-a-well laser applications in analog optical links. IEEE ICTON, pp 1–4
47. Wang KL, Cha D, Liu J, Chen C (2007) Ge/Si self-assembled quantum dots and their optoelectronic device applications. Proc IEEE 95(9):1866
48. Stokes EB, Stiff-Roberts AD, Dameron CT (2006) Quantum dots in semiconductor optoelectronic devices. Electrochem Soc Interface 15:23–27
49. Ren S, Chang L, Lim S, Zhao J, Smith M, Zhao N, Bulovic V, Bawendi M, Gradecak S (2011) Inorganic–organic hybrid solar cell: bridging quantum dots to conjugated polymer nanowires. Nano Lett 11(9):3998–4002
50. De Geyter B et al (2012) Broadband and picosecond intraband absorption in lead-based colloidal quantum dots. ACS NANO 5(1):6067–6074
51. Dabbousi BO, Rodriguez-Viejo J, Mikulec FV, Heine JR, Mattoussi H, Ober R, Jensen KF, Bawendi MG (1997) (CdSe)ZnS core-shell quantum dots: synthesis and characterization of a size series of highly luminescent nanocrystallites. J Phys Chem B 101(46):9463–9475
52. Pechstedt K et al (2010) Photoluminescence of colloidal CdSe/ZnS quantum dots: the critical effect of water molecules. J Phys Chem C 114:12069–12077
53. Zhong S et al (2005) High quality violet to red emitting ZnSe/CdSe core shell nanocrystal. Chem Mater 17(16):4038–4042
54. Pan Z, Zhang H, Cheng K, Hou Y, Hua J, Zhong X (2012) Highly efficient inverted type-I CdS/CdSe core/shell structure QD-sensitized solar cells. ACS Nano 6(5):3982–3991
55. Steckel JS et al (2004) Blue luminescence from (CdS)ZnS Core–shell nanocrystals. Angew Chem Int Ed 43:2154–2158

56. Torchynska TV, Douda J, Sierra RP (2009) Photoluminescence of core-shell CdSe/ZnS quantum dots of different sizes. Phys Status Solidi C 6(S1):S143–S145
57. Li L, Zhang F, Guimard D, Nishioka M, Arakawa Y (2010) 1.3 µm InAs quantum dots grown on silicon substrate. ASOT Conference publication, pp 99–102
58. Farid S, Purahmad M, Stroscio MA, Dutta M (2012) Computational analysis on the emission of ZnO Nanowires and coreshell CdSe/ZnS quantum dots deposited on different substrates. International Workshop on Computational Electronics (IWCE), pp 1–3
59. Luo G, Long J, Zhang B, Liu C, Ji S, Xu J, Yu X, Ni Q (2012) Quantum dots in cancer therapy. 9(1):47–58
60. Zhang H, Yee D, Wang C (2008) Quantum dots for cancer diagnosis and therapy: biological and clinical perspectives. Nanomedicine (Lond) 3(1):83–91
61. Hernández J, Thompson IM (2004) Prostate-specific antigen: a review of the validation of the most commonly used cancer biomarker. Cancer 101(5):894–904
62. Smith AM et al (2006) Multicolor quantum dots for molecular diagnostic of cancer. Expert Rev Mol Diagn 6(2):231–244
63. Medintz IL, Uyeda HT, Goldman ER, Mattoussi H (2005) Quantum dot bioconjugates for imaging, labelling and sensing. Nature Mater 4(6):435–446
64. Dyadyusha L, Yin H, Jaiswal S, Brown T, Baumberg JJ, Booy FP, Melvin T (2005) Quenching of CdSe quantum dot emission, a new approach for biosensing. Chem Commun 25:3201–3203
65. Mansson A, Sundberg M, Balaz M, Bunk R, Nicholls IA, Omling P, Tagerud S, Montelius L (2004) In vitro sliding of actin filaments labelled with single quantum dots. Biochem Biophys Res Commun 314:529–534
66. Wu X, Liu H, Liu J, Haley KN, Treadway JA, Larson JP, Ge N, Peale F, Bruchez MP (2003) Immunofluorescent labeling of cancer marker Her2 and other cellular targets with semiconductor quantum dots. Nat Biotechnol 21:41–46
67. Kaul Z, Yaguchi T, Kaul SC, Hirano T, Wadhwa R, Taira K (2003) Mortalin imaging in normal and cancer cells with quantum dot immuno-conjugates. Cell Res 13:503–507
68. Sukhanova A, Devey J, Venteo L, Kaplan H, Artemyev M, Oleinikov V, Klinov D, Pluot M, Cohen JHM, Nabiev I (2004) Biocompatible fluorescent nanocrystals for immunolabeling of membrane proteins and cells. Anal Biochem 324:60–67
69. Jamieson T, Bakhshi R, Petrova D, Pocock R, Imani M, Seifalian AM (2007) Biological applications of quantum dots. Biomaterials 28:4717–4732
70. Wang YC, Yuan CT, Kuo MY, Wu MC, Jau Tang et al (2012) Enhancement of the Purcell effect for colloidal CdSe/ZnS quantum dots coupled to silver nanowires by a metallic tip. Appl Phys Lett 100:253110
71. Mitchell GP, Mirkin CA, Letsinger RL (1999) Programmed assembly of DNA functionalized quantum dots. J Am Chem Soc 121:8122–8123
72. Chan WC, Nie S (1998) Quantum dot bioconjugates for ultrasensitive nonisotopic detection. Science 281:2016–2018
73. Dahan M, Laurence T, Pinaud F, Chemla DS, Alivisatos AP, Sauer M, Weiss S (2001) Time-gated biological imaging by use of colloidal quantum dots. Opt Lett 26:825–827
74. Chan WCW et al (2002) Luminescent quantum dots for multiplexed biological detection and imaging. Curr Opin Biotechnol 13:40–46
75. Rajh T et al (2004) Charge Transfer across the Nanocrystal-DNA Interface: probing DNA recognition. Nano Lett 4:1017–1023
76. Rajh T, Dimitrijevic NM, Elhofyand A, Rozhkova E (2010) Chapter 4. Biofunctionalized TiO2-based nanocomposites. Handbook of nanophysics. CRC Press, Hoboken, pp 4-1–4–28
77. Lewis FD et al (2008) Getting to guanine: mechanism and dynamic of charge separation and charge recombination in DNA revisited. Photochem Photobiol Sci 7(5):534–539
78. Kanvah S et al (2010) Oxidation of DNA: damage to nucleobases. Acc Chem Res 43(2):280–287
79. Warner WG, Yin JJ, Wei RR (1997) Oxidative damage to nucleic acids photosensitized by titanium dioxide. Free Radic Biol Med 23:851

80. Paunesku T et al (2003) Biology of TiO2-oligonucleotide nanocomposites. Nat Mater 2(5):343–346
81. Enders PJ, Paunesku T, Vogt S, Meade TJ, Woloschak GE (2007) DNA-TiO2 nanoconjugates Labeled with magnetic resonance contrast agents. J Am Chem Soc 129(51):15760–15761
82. Vasudev M et al (2008) Optoelectronic signatures of biomolecules including hybrid nanostructure-DNA ensembles. IEEE Sensors J 8(6):743–749
83. Ramadurai D et al (2007) Interactions of THz vibrational modes with charge carriers in DNA: Polaron-Phonon interactions. Int J High Speed Electron Syst 17(2):293–309
84. Ramadurai D et al (2008) Environmental effects influencing the vibrational modes of DNA: nanostructures couples to biomolecules. Int J High Speed Electron Syst 18(1):47–61
85. Stroscio MA, Dutta M (2001) Phonons in nanostructures. Cambridge University Press, Cambridge
86. Meshik X, Brenneman K, Xu K, Ranginwala S, Abell J, Zhao Y, Dutta M, Stroscio M (2012) Surface-enhanced raman spectroscopy signatures of an RNA molecule: an aptamer that binds to αVβ3 integrin. AIP Conf Proc 1506:49–52
87. Mi J, Zhang Z, Giangrande PH, McNamara JO II, Nimjee SM, Sarraf-Yazdi S, Sullenger BA, Clary BM (2005) Targeted inhibition of αVβ3integrin with an RNA aptamer inpairs endothelial cell growth and survival. Biochem Biophys Res Commun 228:956–963
88. Chaney SB, Shanmukh S, Dluhy RA, Zhao Y-P (2005) Aligned silver nanorod arrays produce high sensitivity surface-enhanced raman spectroscopy substrates. Appl Phys Lett 87:031908
89. Otto C, Van Den Tweel TJJ, de Mul FFM, Greve J (1986) Surface-enhanced Raman spectroscopy of DNA bases. J Raman Spec 17:289–298
90. Biese B, McNaughton D (2002) Surface-enhanced Raman spectroscopic study of uracil. The influence of the surface substrate, surface potential, and pH. J Phys Chem B 106:1461–1470
91. Vasudev M, Wu T-C, Bitwas S, Dutta M, Stroscio MA, Guthrie S, Reed M, Burris KP, Stewart CN Jr (2001) Optoelectronic signatures of DNA-based hybrid nanostructures. IEEE Trans Nanotechnol 10:35–43
92. Wang J, Gudiksen MS, Duan X, Cui Y, Lieber CM (2001) Science 293:1455
93. Kong KJ, Franklin N, Zhou C, Chapline M, Peng S, Cho K, Dai H (2000) Science 287:622
94. Sarkar J, Khan GG, Basumallick A (2007) Bull Mater Sci 30(3):271–290
95. Kumar C (ed) (2007) Nanomaterials for biosensors. Wiley-VCH, Weinheim
96. Friedman AL, Menon L (2007) J Elec Soc 154(4):E68–E70
97. Menon L (2003) Synthesis of quantum wires using porous alumina. In: Bandyopadhyay S, Nalwa H (eds) Quantum Dots and Quantum Wires, American Scientific Publishers, pp 142–191: ISBN: 1-58883-013-6
98. Alivisatos AP (1996) J Phys Chem 100:13226–13239
99. Landau LD, Lifshitz EM, Pitaevskii LP (1984) Electrodynamics of continuous media. Pergamon, Oxford, pp 34Ð42
100. Ruda HE, Shik A (2005) Physical Rev B 72:115308
101. Empedocles SA, Norris DJ, Bawendi MG (1996) Phys Rev Lett 77:3873
102. Vouilloz F et al (1998) Phys Rev B 57:12378
103. Akiyama H, Someya T, Sakaki H (1996) Phys Rev B 53:R4229
104. Ils P et al (1995) Phys Rev B 51:4272
105. Liu P, Singh VP, Jarro CA, Rajaputra S (2011) IOP Sci Nanotechnol 22:145304 (9 pp)
106. Duan X, Huang Y, Cui Y, Wang J, Lieber CM (2001) Nature 409:66
107. Huang Y, Duan X, Wei Q, Lieber CM (2001) Science 291:630
108. Cui Y, Lieber CM (2001) Science 291:851
109. Kim SN, Kuang Z, Slocik JM, Jones SE, Cui Y, Farmer BL, McAlpine MC, Naik RR (2011) Preferential binding of peptides to graphene edges and planes. J Am Chem Soc 133(37):14480–14483
110. Tomaisio SM, Walsh TR (2009) Modeling the binding affinity of peptides for graphitic surfaces; influences of aromatic content and interfacial shape. J Phys Chem C 113:8778–8785

111. Kuang Z, Kim SN, Crookes-Goodson WJ, Farmer BL, Naik RR (2010) Biomimetic chemosensor: designing peptide recognition elements for surface functionalization of carbon nanotube field effect transistors. ACS Nano 4(1):452–458
112. Lu CH, Li J, Zhang XL, Zheng AX, Yang HH, Chen X, Chen GN (2011) General approach for monitoring peptide-protein interactions based on graphene-peptide complex. Anal Chem 83:7276–7282
113. Oh KJ, Cash KJ, Plaxco KW (2006) Excimer-based peptide beacons: a convenient experimental approach for monitoring polypeptide-protein and polypeptide-oligonucleotide interactions. J Am Chem Soc 128(143):14018–14019
114. Geim AK (2009) Graphene: status and prospects. Science 324:1530–1534
115. Xu Y, Bai H, Lu G, Li C, Shi G (2008) Flexible graphene films via the filtration of water-soluble noncovalent functionalized graphene sheets. J Am Chem Soc 130(18):5856–5857
116. So CR, Hayamizu Y, Yazici H, Gresswell C, Khatayevich D, Tamerler C, Sarikaya M (2012) Controlling self-assembly of engineered peptides on graphite by rational mutation. ACS Nano 6(2):1648–1656
117. Katoch J, Kim SN, Kuang Z, Farmer BL, Naik RR, Tatulian SA, Ishigami M (2012) Structure of a peptide adsorbed on graphene and graphite. Nano Lett 12:2342–2346
118. Cui Y, Kim SN, Jones SE, Wissler LL, Naik RR, McAlpine MC (2010) Chemical functionalization of graphene enabled by phage displayed peptides. Nano Lett 10(11):4559–4565
119. Wang S, Humphreys ES, Chung SY, Delduco DF, Lustig SR, Wang H, Parker KN, Rizzo NW, Subramoney S, Chiang YM, Jagota A (2003) Peptides with selective affinity for carbon nanotubes. Nature 2:196–200
120. Acevedo AO, Xie H, Zorbas V, Sampson WM, Dalton AB, Baughman RH, Draper RK, Musselman IH, Dieckmann GR (2005) Diameter-selective solubilization of single-walled carbon nanotubes by reversible cyclic peptides. J Am Chem Soc 127:9512–9517
121. Lopez SF, Kim HS, Choi EC, Delgado M, Granja JR, Khasanov A, Kraehenbuehl K, Long G, Weinberger DA, Wilcoxen KM (2011) Antibacterial agents based on the cyclic D, L-peptide architecture. Nature 412:425–455
122. Wang X, Wang C, Qu K, Song Y, Ren J, Miyoshi D, Sugimoto N, Qu X (2010) Ultrasensitive and selective detection of prognostic indicator in early-stage cancer using graphene oxide and nanotubes. Adv Funct Mater 20:3967–3971
123. Song Y, Qu K, Zhao C, Ren J, Qu X (2010) Graphene oxide: intrinsic peroxidase catalytic activity and its application to glucose detection. Adv Mater 22:2206–2210
124. Rajesh C, Majumder C, Mizuseki H, Kawazoe Y (2009) A theoretical study on the interaction of aromatic amino acids with graphene and single walled carbon nanotube. J Chem Phys 130:124911
125. Pantarotto D, Partidos CD, Graff R, Hoebeke J, Briand JP, Prato M, Bianco A (2003) Synthesis, structural characterization, and immunological properties of carbon nanotubes functionalized with peptides. J Am Chem Soc 125:6160–6164
126. Huan TN, Ganesh T, Han SH, Yoon MY, Chung H (2011) sensitive detection of an antharax biomarker using a glassy carbon electrode with consecutively immobilized layer of polyalinine/carbon nanotube/peptide. Biosens Bioelectron 26:4227–4230
127. Huan TN, Ha VTT, Hung LQ, Yoon MY, Han SH, Chung H (2009) Square wave voltammetric detection of antharax utilizing a peptide for selective recognition of a protein biomarker. Biosens Bioelectron 25(2):469–474
128. Mirzaei M, Meskinfam M, Yousefi M (2012) Covalent hybridizations of carbon nanotubes through peptide linkages: a density functional approach. Comput Theoretical Chem 981:47–51
129. West PR, Ishii S, Naik GV et al (2010) Searching for better plasmonic materials. Laser Photonics Rev 4(6):795–808
130. Moskovits M (2005) Surface-enhanced Raman spectroscopy: a brief retrospective. J Raman Spectrosc 36(6–7):485–496
131. Chaney SB, Shanmukh S, Dluhy RA et al (2005) Aligned silver nanorod arrays produce high sensitivity surface-enhanced Raman spectroscopy substrates. App Phys Lett 87(3):3

132. Willets KA, Van Duyne RP (2007) Localized surface plasmon resonance spectroscopy and sensing. Annual review of physical chemistry. Annual Reviews, Palo Alto, pp 267–297
133. Shafer-Peltier KE, Haynes CL, Glucksberg MR et al (2003) Toward a glucose biosensor based on surface-enhanced Raman scattering. J Am Chem Soc 125(2):588–593
134. Yonzon CR, Stuart DA, Zhang XY et al (15 September 2005) Towards advanced chemical and biological nanosensors—an overview. Talanta 67(3):438–448
135. Yonzon CR, Jeoungf E, Zou SL et al (2004) A comparative analysis of localized and propagating surface plasmon resonance sensors: the binding of concanavalin a to a monosaccharide functionalized self-assembled monolayer. J Am Chem Soc 126(39):12669–12676
136. Chien F-C, Huang WY, Shiu J-Y et al (2009) Revealing the spatial distribution of the site enhancement for the surface enhanced Raman scattering on the regular nanoparticle arrays. Opt Express 17(16):13974–13981
137. Shanmukh S, Jones L, Driskell J et al (2006) Rapid and sensitive detection of respiratory virus molecular signatures using a silver nanorod array SERS substrate. Nano Lett 6(11):2630–2636
138. Li J, Fattal D, Li Z (2009) Plasmonic optical antennas on dielectric gratings with high field enhancement for surface enhanced Raman spectroscopy. Appl Phys Lett 94(26):263114
139. Lee YH, Dai S, Young JP (1997) Silver-doped sol-gel films as the substrate for surface-enhanced Raman scattering. J Raman Spectrosc 28(8):635–639
140. Huang Y, Yang Y, Chen Z et al (2008) Fabricating Au-Ag core-shell composite films for surface-enhanced Raman scattering. J Mater Sci 43(15):5390–5393
141. Kahraman M, Aydin O, Culha M (2009) Oligonucleotide-mediated Au-Ag core-shell nanoparticles. Plasmonics 4(4):293–301
142. Yang Y, Xiong LM, Shi JL et al (2006) Aligned silver nanorod arrays for surface-enhanced Raman scattering. Nanotechnology 17(10):2670–2674
143. Liu YJ, Zhang ZY, Dluhy RA et al (2010) The SERS response of semiordered Ag nanorod arrays fabricated by template oblique angle deposition. J Raman Spectrosc 41(10):1112–1118
144. Zhao LL, Kelly KL, Schatz GC (2003) The extinction spectra of silver nanoparticle arrays: influence of array structure on plasmon resonance wavelength and width. J Phy Chem B 107(30):7343–7350
145. Brenneman KL, Meshik X, Xu et al (2012) Surface-enhanced Raman spectroscopy study of single stranded DNA sequences on silver nanorod array, PHONONS 2012, AIP Conf. Proc. 1506, pp 53–56; doi: 10.1063/1.4772525
146. Shang Z-G, Ting DN, Wong YT et al (2007) A study of DFT and surface enhanced Raman scattering in silver colloids for thymine. J Mol Struct 826(1):64–67
147. Shang Z, Gao Y, Jia T et al (2009) Vibrational modes study of thymine on the surface of copper electrode using SERS-measurement and the DFT method. J Mol Struct 930(1–3):60–64